The Influence of Materials and Fabrication Techniques on Dye-sensitized Solar Cell Performance

Daniel J. Myers

A thesis
submitted in partial fulfillment of the
requirements for the degree of

MASTER OF SCIENCE IN ENGINEERING

(MECHANICAL ENGINEERING)

University of Washington

2012

Reading Committee:

Guozhong Cao, Chair

Qifeng Zhang, Chair

Steve Shen

Junlan Wang

Program Authorized to Offer Degree:
Department of Mechanical Engineering

University of Washington

Abstract

The Influence of Materials and Fabrication Techniques on Dye-sensitized Solar Cell Performance

Daniel J. Myers

Co-Chairs of the Supervisory Committee:
Professor Guozhong Cao
Material Science and Engineering

Research Assistant Professor Qifeng Zhang
Material Science and Engineering

The performance of dye-sensitized solar cells (DSC) as reported in the literature varies even when the materials and/or methods cited are essentially the same. DSC performance even varies significantly within a single lab from researcher to researcher, as has been observed in our lab. To better constrain the sources of the variability and determine which materials and techniques yielded the best DSC performance, various materials and techniques for fabrication of dye-sensitized solar cells were evaluated for their effect on DSC performance. Materials investigated included two types of TiO_2 nanoparticles (Aeroxide® P25 and a nanoparticle synthesized in our lab) as well as two different electrolytes (Dyesol's High Performance Electrolyte and an electrolyte synthesized in our lab). Results in the literature suggest that nanoparticle dispersion during screen printing paste fabrication is important for the dye loading and optical properties of DSCs, so dispersion techniques including mortar grinding, sonication, roller milling, and ball milling were investigated. DSC fabrication and assembly techniques were also suspected to be important. Comparisons were made between doctor bladed and screen printed films, dye loading of the TiO_2 film under ambient pressures and vacuum, and various sealed and unsealed cell testing configurations.

Results from the material and assembly technique comparisons showed varying degrees of impact on DSC film quality and performance. Ball milling was found to be an effective method of disaggregating P25 TiO_2 nanoparticles for screen printing pastes, whereas mortar grinding left large TiO_2 clusters and yielded variable cluster size distributions from batch to batch. The presence of TiO_2 clusters increased film cracking, film peeling, and light scattering and consequently reduced DSC performance. Vacuum-assisted dye loading was not found to improve DSC performance. A comparison of gasket-sealed, epoxy-sealed, and unsealed DSCs did not show consistent differences in performance, though unsealed cells showed poor stability over short time periods. Both screen printing and doctor blading of TiO_2 films yielded films of uniform thickness and DSCs of comparable performance. Finally, a lab electrolyte was found to yield DSCs with a higher short circuit current compared to DSCs that used Dyesol's High Performance Electrolyte. The electrolyte performance difference is partially due to higher charge transfer resistance at the TiO_2-electrolyte interface.

TABLE OF CONTENTS

Page

List of Figures iii

List of Tables v

Acknowledgments i

Chapter 1: Introduction 1
1.1 PV History 2
1.2 DSC Structure and Function 3
1.3 DSC Characteristics 7
1.4 DSC Fabrication Techniques 9
1.5 Objectives and Scope 11

Chapter 2: Experimental 13
2.1 Materials 13
2.2 Methods 15
2.2.1 Paste Fabrication 15
2.2.2 Working Electrode Fabrication 16
2.2.3 Cell Assembly 22
2.3 DSC Characterization 28
2.3.1 J-V Curves 28
2.3.2 Electrochemical Impedance Spectroscopy 30
2.3.3 Film Area and Thickness Measurements 33
2.3.4 Dynamic Light scattering 34

Chapter 3: Results and Conclusions 37
3.1 Influences of Film Structure 37

3.1.1 Paste Preparation Methods 37
3.1.2 Uniformity of Doctor Bladed Films 49
3.1.3 Comparison of Films Created Using Doctor Blade and Screen Printing Techniques 52
3.2 Influences of Device Structure and Assembly 52
3.2.1 Vacuum Dye Loading 52
3.2.2 Sealing 56
3.2.3 Electrolytes 57
3.3 Conclusions 66
3.3.1 Preparation of the Photoanode Film 67
3.3.2 Device Assembly 70

References 73

LIST OF FIGURES

Figure Number		Page
1.1	Typical structure of a DSC showing the random walk of electron diffusing through the SMO network.	5
1.2	Processes occurring within a DSC by energy level.	6
1.3	Example performance data for a DSC.	8
1.4	Solar cell equivalent circuit.	9
2.1	Powder XRD spectra for P25 and lab nanoparticles.	14
2.2	TiO_2 paste preparation procedures.	17
2.3	Screen printing station.	20
2.4	Squeegees and relaxation chamber.	21
2.5	Smoothing gasket onto the substrate with stir rod. Smoothing gasket helps achieve rapid sealing without gaps in the seal.	24
2.6	Setup of hot platen press for DSC sealing with thermoplastic gasket.	26
2.7	Epoxy-sealed DSC.	27
2.8	Cell in vacuum chamber for electrolyte infiltration.	27
2.9	Sealing of electrolyte infiltration hole.	28
2.10	DSC mounting for J-V testing.	30
2.11	DSC in mount with weigh paper spacer for open testing.	31
2.12	Image processing of scanned TiO_2 film to measure film area.	35
3.1	Particle size distribution for mortar ground pastes with and without roller milling.	40
3.2	Optical microscope images of films made from mortar ground and roller milled pastes.	41
3.3	Agglomerate of P25 formed in aqueous dispersion.	42
3.4	Particle size distributions for ball milled P25 pastes.	43
3.5	Optical microscope images of films made from mortar ground, mortar ground and roller milled, and ball milled pastes.	46

3.6 SEM images of films made from mortar ground, mortar ground and roller milled, and ball milled pastes. 47
3.7 UV-Vis spectra of films made from mortar ground, mortar ground and roller milled, and ball milled pastes. 48
3.8 Particle size distributions for pastes PB42a, PB44, and PB46 shown as number fraction. 49
3.9 Profile directions for contact profilometer measurements of film thickness relative to doctor blade direction. 50
3.10 Thickness profiles of doctor bladed film sets a , b, and c. 51
3.11 Longitudinal film thickness profiles of screen printed and doctor bladed films. 53
3.12 Transverse film thickness profiles of screen printed and doctor bladed films. 54
3.13 Stability of performance for heat sealed and unsealed DSCs. 57
3.14 J-V plot for initial comparison of lab and Dyesol HPE1 electrolytes. . 59
3.15 Nyquist plot for TiO_2-Pt cells. 61
3.16 Equivalent circuit used to fit impedance data for the TiO_2-Pt cells. . 62
3.17 Example of equivalent circuit fit to impedance data for the circuit shown in Figure 3.16. 63
3.18 Nyquist plot for Pt-Pt cells. 64
3.19 Equivalent circuit fit to impedance data for the Pt-Pt cells. 65

LIST OF TABLES

Table Number		Page
1.1	Comparison of P25-based DSC performances in the literature.	11
2.1	Effect of TiO_2 film area measurement method on DSC performance measures.	36
3.1	Dispersion techniques used for pastes.	39
3.2	Performance data for films made from pastes of varying particle size distributions from different dispersion techniques.	45
3.3	Comparison of the performance of screen printed and doctor bladed films.	55
3.4	Performance of DSCs that underwent vacuum dye loading and dye loading at atmospheric pressure.	55
3.5	Performance of unsealed, heat sealed, and epoxy sealed DSCs.	56
3.6	Performance data for initial comparison of lab and Dyesol HPE1 electrolytes.	58
3.7	Performance data for second comparison of lab, Dyesol HPE1, and HPE2 electrolytes.	60
3.8	Results of EIS testing of the three electrolytes.	66

ACKNOWLEDGMENTS

This work could not have been completed without the assistance of numerous individuals. Dr. Guozhong Cao and Dr. Qifeng Zhang provided financial support as well as invaluable feedback and guidance on my research. Dr. Junlan Wang and Dr. Steve Shen also served on my committee and reviewed my work. Several professors provided access to instruments and equipment in their labs including Dr. Christine Luscombe, Dr. Samson Jenekhe, and Dr. Alex Jen. Dr. Jeffery Stevenson and Ryan Scott assisted with work carried out at Pacific Northwest National Lab. Dr. Seigo Ito at the University of Hyogo, Japan answered my long list of questions about fabricating screen printing pastes for dye-sensitized solar cell fabrication. Tuesday Kuykendall assisted with access and training to use Material Science Department equipment, as did Paul Schilling for equipment at the University of Washington Microfabrication Facility. Matt Ferguson, Peter Kazarinoff, and Pinyi Yang also assisted with experiments and provided useful suggestions. And last, but not least, the other members of the Sol-Gel Lab were always willing to lend assistance when I asked for it, and created a friendly environment in which to work.

This work was supported by the following grants:

- U.S. Department of Energy, Office of Basic Energy Sciences, Division of Materials Sciences, Award no. DE-FG02-07ER46467 (Q.F.Z.)

- National Science Foundation (DMR 1035196, DMR-0605159 and CMMI-1030048)

- Royalty Research Fund (RRF) from the Office of Research at University of Washington

- Trans-Pacific Fellowship, University of Washington and the University of Queensland, Australia

Chapter 1

INTRODUCTION

Humanity faces a number of global challenges as we progress into the 21st century. Some of these challenges relate to the scarcity of resources including water and food, while others concern maintaining the quality of the global environment by addressing problems such as global climate change and pollution of air, soil, and water [44]. These are a complex set of interrelated problems, with solutions to one problem alleviating and/or exacerbating other problems. Thus, solutions to these problems cannot be considered in isolation and must account for their impacts to other global issues.

The future sources of energy to power our modern lifestyle and economies is a member of this set of challenges. Long term questions remain about where we will obtain the energy to fuel our cars, power our factories, and light our homes as fossil fuel supplies dwindle and the environmental costs associated with their use become unacceptable. The candidate energy sources to replace fossil fuels include renewable (hydropower, wind, solar, tidal, geothermal, and biofuels) and nuclear energy. Each energy source has its own set of challenges and potential impacts on the other great challenges. For example, while biofuels have the potential to be carbon neutral and thus help ameliorate global climate change, many biofuels under consideration will be produced on the same land as food crops, thus displacing those food crops and increasing food prices [42]. Biofuel production may also consume scarce water resources and may need fertilizers that can pollute surface waters [20].

Of the potential energy sources to offset our diminished use of fossil fuels, solar energy has a number of attractive features [4]. The fuel resource (sunlight), is free and widely available. Solar has virtually no risk of large scale, catastrophic accidents

as is the case for nuclear and large-scale hydropower. While solar thermal plants may require water for cooling purposes, photovoltaic (PV) solar panels require no water except to occasionally clean the panels. As with any energy source, solar has its own set of drawbacks including the intermittent nature of sunshine, the large areas of land required to harvest large quantities sunlight, and the current high cost of solar energy when compared to other energy sources. However, the benefits of solar energy and the prospect that some of its disadvantages can be addressed with better technology means that it will likely make up a significant share of our future energy supply mix.

1.1 PV History

This thesis focuses on the fabrication of one particular type of PV solar cell: the dye-sensitized solar cell (DSC). The DSC is one of the so-called third generation photovoltaic solar cells [12]. The first generation consists of the traditional mono- and polycrystalline silicon P-N junction solar cell and trace their initial development back to efforts at Bell Research Labs in the 1950's [6]. While traditional silicon PV cells are a proven technology with efficiencies around 20% and are very durable, their high production cost continues to limit their widespread adoption. The high cost of traditional silicon stems from the high labor, material, and energy requirements required to produce them [11]. Traditional silicon PV cells are also relatively fragile, and cannot be used in applications where flexibility is important.

To address the issues of the silicon wafer solar cell, a second generation of thin film cells was developed [11]. This second generation of cells include a number of different materials such as amorphous silicon, copper-indium-gallium-selenide (CIGS), and cadmium-telluride (CdTe). The thin film technologies require less material to manufacture, can be made on flexible substrates, and require less energy to manufacture. These advantages, however, have not significantly dropped the price of PV using thin film technologies, and the thin film cells tend to have lower efficiencies than the traditional silicon cells. There are also concerns about the continued availability

of rare earth metals required for some of the technologies, as well as the toxicity of the other components of the thin film cells, most notably cadmium.

The third generation of cells include a number of different technologies including quantum dot [13, 14], hot carrier [13, 14], polymer [27], and dye-sensitized solar cells. In particular, polymer solar cells (PSCs) and DSCs show great promise for relatively low production costs. Both PSCs [3] and DSCs [43] can be made in a flexible format, and so should be amenable to roll-to-roll processing techniques that should lower costs. With the exception of the dyes used in the DSCs, the other materials used in DSC construction are inexpensive and widely available.

Many challenges with PSC and DSC technologies remain to be solved before they can be adopted for large-scale power production. The published record efficiencies for lab-scale PSCs and DSCs as of this writing are 8.6% and 12.3% respectively [51, 8], and PSC and DSC efficienies drop significantly when scaled up and assembled into modules. The resulting efficiencies are well below the performance of traditional first generation silicon PV modules. The durability PSCs and DSCs also pales in comparison to that of silicon PV cells [29, 27]. The potential benefits of these third generation PV technologies, however, continues to motivate research and development efforts to overcome these issues.

1.2 DSC Structure and Function

An understanding of the functioning of the DSC can be gained by considering the traditional DSC structure [34] shown in Figure 1.1. The cell consists of a photoanode (working electrode) and cathode (counter electrode) separated by a gap. The photoanode is a mesoporous, semiconducting metal oxide (SMO) film, usually zinc oxide (ZnO) or titanium dioxide (TiO_2), coated onto a conductive substrate. A light-sensitive dye is adsorbed onto the SMO film. The cathode consists of a catalytic film, usually carbon [28, 38] or platinum [34], coated onto another conductive substrate. The photoanode, cathode, or both electrodes will be transparent depending on the di-

rection of illumination. As the transparent substrates are often non-conductive glass, a transparent conductive oxide (TCO) layer is deposited on the non-conductive substrate. Common TCO films are fluorine-doped tin oxide (FTO) and indium-doped tin oxide (ITO). The cell gap is maintained by a spacer and filled with an electrolyte. The electrolyte also penetrates the SMO film on the photoanode. The ions in the electrolyte make up a redox couple that will be oxidized at the photoanode and reduced at the cathode. The most commonly used DSC electrolyte consists of the iodide/triiodide (I^-/I_3^-) redox couple.

The processes occurring within the DSC can be understood by considering the energy levels of the materials within the cell as shown in Figure 1.2 [12]. When an incoming photon is absorbed by the dye molecule, it excites an electron (1) that enters the conduction band of the SMO(2), the charge injection process occurring on pico/femto second timescale [19]. The exited electron then diffuses through the SMO film to the conductive substrate and out of the cell to perform electrical work. The electron lost by the dye molecule is replaced by an electron from I^- (3). The resulting I_3^- diffuses back to the cathode and is reduced to I^- by electrons flowing into the cathode (4), thus forming a complete electrical circuit. The difference between the redox potential E_R and the Fermi level in the mesoporous semiconductor E_F determines the maximum possible value for the cell voltage V.

There are a variety of designs of DSCs currently underdevelopment. Different substrates are being investigated including electrically conductive plastics [21], metal foils [36], and metal meshes [18, 39]. This thesis will address the traditional DSC structure with one photoanode and one cathode, the former consisting of a mesoporous TiO_2 film on an FTO glass substrate, and the later of a mesoporous platinum film-coated FTO glass substrate. The electrolytes used are based on the iodide-triiodide redox couple. The dye used was the ruthenium-based N719 dye.

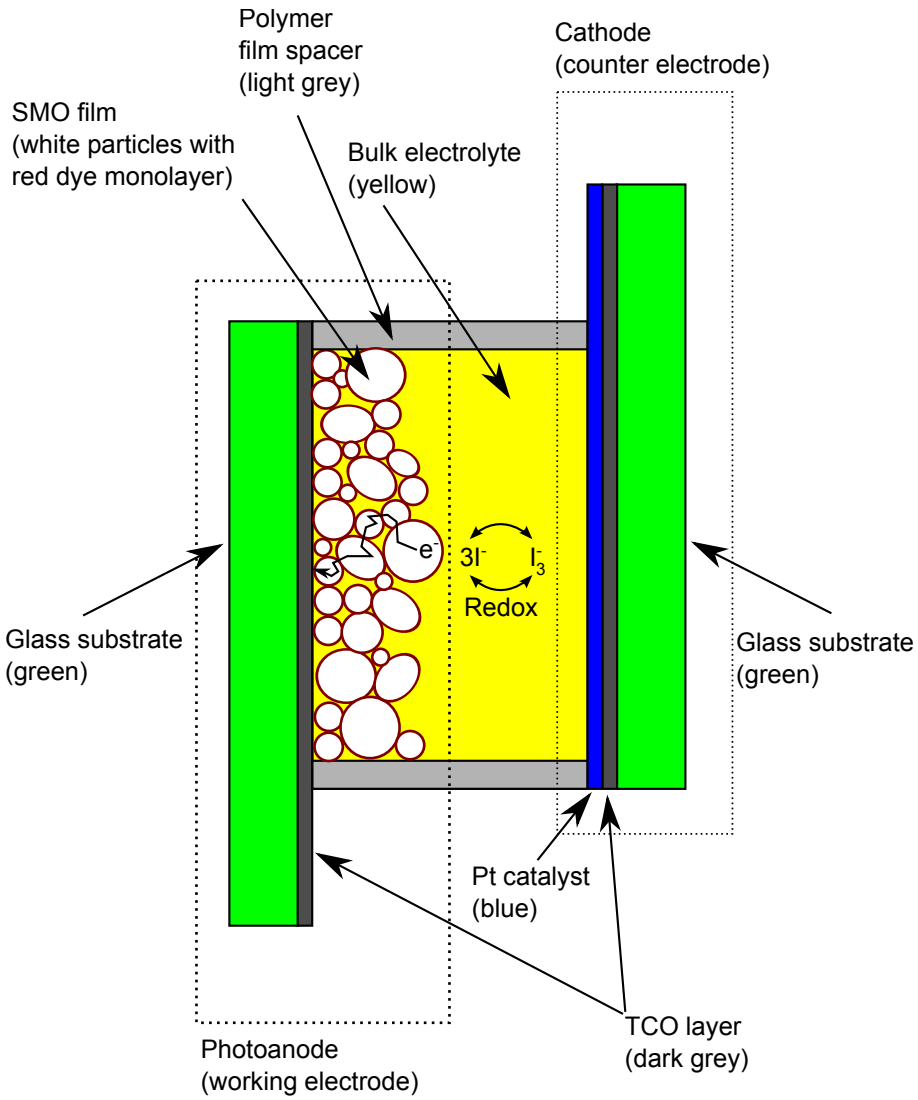

Figure 1.1: Typical structure of a DSC showing the random walk of electron diffusing through the SMO network.

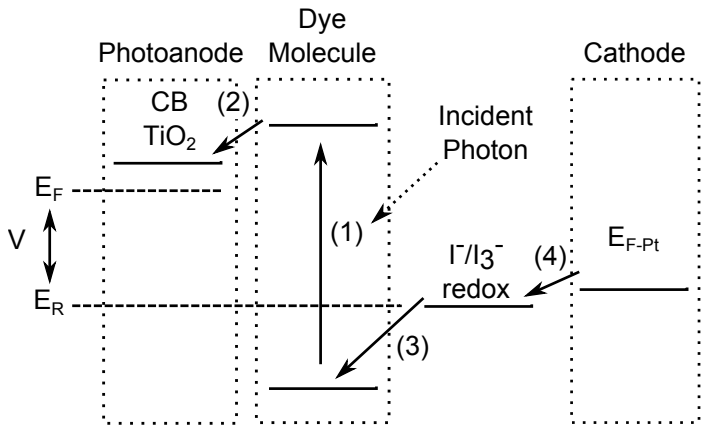

Figure 1.2: Processes occurring within a DSC by energy level. CB TiO_2 and $E_{F\text{-}Pt}$ are the conduction band and Fermi energy levels of the TiO_2 network and platinum layer on the cathode respectively. E_F is the Fermi level in the TiO_2 layer and E_R is the redox potential of the I^-/I_3^- redox couple. Solid arrows represent the path of electrons between energy levels. V is the potential difference between the TiO_2 Fermi level and the electrolyte redox potential. Recombination reactions are not shown.

1.3 DSC Characteristics

The basic measure of performance for photovoltaic devices including silicon, thin film, polymer, and DSC cells is the current density versus voltage curve (J-V curve). An example of such a curve is shown in Figure 1.3a. From the J-V curve, the following cell characteristics can be found directly: the open circuit voltage (V_{oc}) and the short circuit current density (J_{sc}). By calculating the power density versus voltage curve from the current density and cell voltage as shown in Figure 1.3b, the peak power density (P_{max}) can be found.

The fill factor (ff) for the cell is then calculated as follows:

$$ff = \frac{P_{max}}{V_{oc} \cdot J_{sc}}$$

On the J-V curve, the ff is the ratio of the areas of the P_{max}(grey) and $V_{oc} \times J_{sc}$ (dashed) boxes shown in Figure 1.3a. The cell efficiency (η) is defined by taking the ratio of P_{max} to the incident light intensity. When the units of P_{max} are given as milliwatts/cm^2 and the incident light intensity is the standard 100 milliwatts/cm^2, then the values for P_{max} and η are the same.

Each of the performance measures relates to a particular characteristic of the DSC. The V_{oc} is determined by the difference between the Fermi level, E_F, in the SMO film and the redox potential of the redox couple in the electrolyte when no current is flowing through the cell. The value of E_F in turn is determined by factors that affect the concentration of electrons in conduction band of the SMO film at open circuit. These factors include the dye charge injection efficiency and the recombination rate of electrons in the conduction band or trapped states with I_3^- ions in the electrolyte or the oxidized dye molecule [33]. The J_{sc} reflects the intensity of the incident light, reflection and absorption light losses due to the substrate, the absorption efficiency of the dye, the dye injection efficiency, and the recombination rate.

The meaning of the fill factor can be understand by considering the equivalent

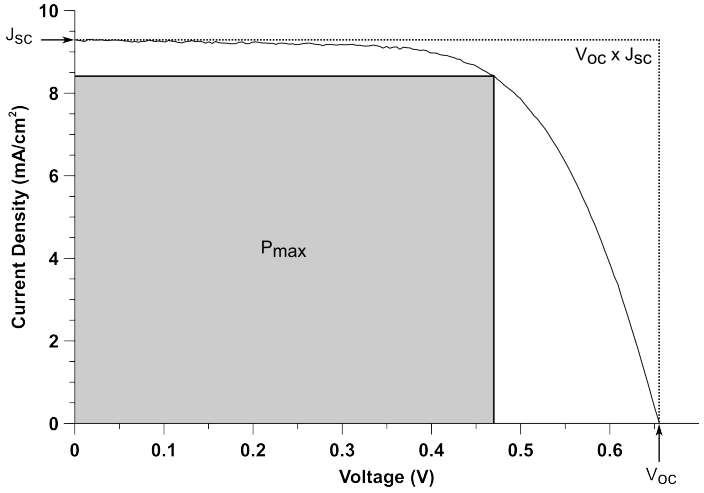

(a) Example J-V curve including areas denoting P_{max} and $V_{oc} \times J_{sc}$.

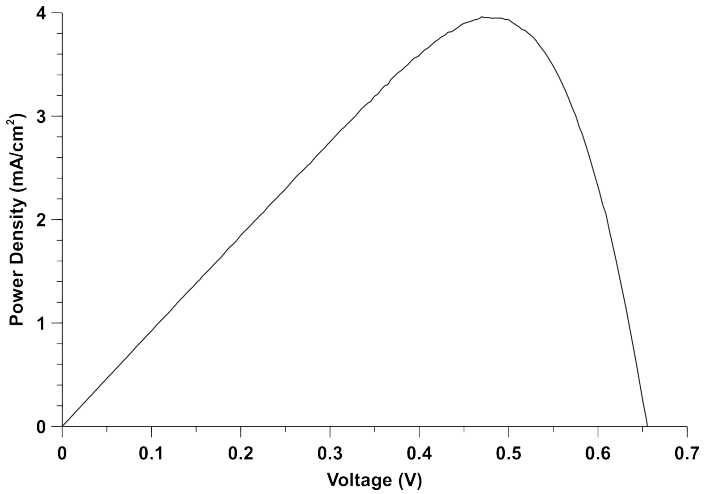

(b) P-V curve.

Figure 1.3: Example performance data for a DSC.

circuit for a photodiode. Any photodiode can be represented by the equivalent circuit shown in Figure 1.4 consisting of a current source, a diode, a shunt resistance R_{sh}, and a series resistance R_s. The fill factor reflects the R_s of the DSC: the higher the

R_s, the lower the fill factor. The R_s value of a DSC is influenced by many factors including the sheet resistance of the TCO film on the substrates, the conductivity of the electrolyte, the surface area of the electrodes, and the cell gap.

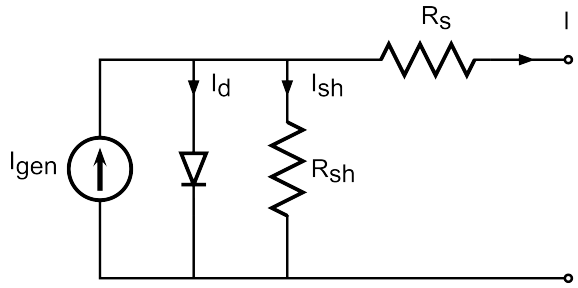

Figure 1.4: Solar cell equivalent circuit. I_{gen} is the photocurrent, I_d is the diode current, I_{sh} is the shunt current, R_{sh} is the shunt resistance, R_s is the series resistance, and I is the output current of the cell.

The overall efficiency of a DSC, η, is influenced by the factors cited above, as well as other aspects of the cells design. Reflective light losses off the front surface of the DSC and transmission losses through the back of the DSC will clearly reduce the efficiency. The absorption spectrum of the dye will determine how much of the incident light actually generates excited electrons in the dye and which incident wavelengths of light will be lost. While relatively unimportant for the cells tested in this research with ~5 mm by ~5 mm TiO_2 films, the geometry of the external electrical connection to the DSC will impact the current paths through the cell and thus the R_s value. Indeed, the larger the area of the cell, the more important the sheet resistance of the TCO film becomes in determining R_s and in turn η.

1.4 DSC Fabrication Techniques

The techniques used to fabricate and test DSCs as reported in the literature are varied. Both doctor blade [30, 47, 23] and screen printing [22, 10, 43] techniques have

been used to make the films. While many researchers test their DSCs in a sealed configuration where a gasket [22] or epoxy [39] seals the edges of the cell [22, 47], others test their DSCs in an open configuration [7]. There is no direct comparison of the effects of these fabrication techniques DSC performance available in the literature, however.

The dye loading procedure used for TiO_2 film-based DSCs is fairly uniform in the literature. Researchers using N719 dye commonly immerse their DSC films in a 0.5 mM solution with either ethanol [32] or a 50/50 mixture of tert-butanol and acetonitrile [22] as the solvents. Dye loading times are on the order of 24 hours. In order for effective dye loading to take place, the dye must penetrate the TiO_2 film completely. This requirement suggests that incomplete penetration of the dye into the pores of the film would reduce dye loading and DSC performance. Conceivably, incomplete penetration of the dye could occur if gas were trapped in the pores of the film during dye loading. Such trapped gases could be removed by exposing the films to reduced pressure during dye loading, though a test of this technique has not been reported.

A wide variety of paste fabrication techniques are in use. When pastes are formulated from nanoparticles in dried form, the nanoparticles must be disaggregated before forming a paste. Disaggregation techniques include mortar grinding [22, 25], ball milling either in standard ball mills or high velocity bead mills [25, 50], sonication [22, 25, 50], chemical treatment [25, 23], or some combination of the above methods. The different nanoparticle dispersion methods lead to varying degrees of disaggregation and, in turn, variations in dye loading and DSC performance [25, 50].

In addition to its effect on dye loading, a potential mechanism by which disaggregation can impact DSC performance is through its role in crack formation. Ito and others [22] reported that aggregates seem to be associated with cracking and peeling of the TiO_2 films made from commercially available nanoparticles. Other researchers [10, 30] investigated the effect of paste ethyl cellulose content on crack

formation. We were unable, however, to find studies showing a link between the degree of crack formation and particle aggregation.

1.5 Objectives and Scope

Given the variety of techniques used to fabricate DSC materials and devices presented in the literature, it is difficult to know which techniques are best to use. Different labs using similar techniques and materials obtain varying DSC performances. Table 1.1 shows performance results for P25 Aeroxide® cells. Cell efficiencies range from 3.4% to 10.1%. The cells with the two highest performances included $TiCl_4$ treatments, scattering layers, and anti-reflective coatings to boost performance. Among the other cells without the performance enhancing treatments, most cell efficiencies seem to cluster around ∼6%. This suggests that 6% efficiency is a reasonable performance goal for a well constructed P25-based, single layer DSC.

Reference	Dispersion Technique	Film Deposition Technique	Jsc (mA/cm2)	Voc (V)	FF	Efficiency (%)
Yamamoto et al., 2011 [48]	Bead mill	Screen Print	18.0	0.795	0.704	10.1
Ito et al., 2007 [21]	Mortar grinding, sonication, roller milling	Screen Print	16.25	0.779	0.730	9.24
Ito et al., 2003 [22]	Chemical	Doctor Blade	12.2	0.690	0.71	6.0
Adachi et al., 2006 [1]	Not specified	Not specified	6.81	0.760	0.71	6.09
Liberatore et al., 2009 [30]	Not specified	Doctor Blade	6.90	0.75	0.64	3.4
Xu et al., 2011 [47]	Attritor Mill	Doctor Blade	12.8	0.710	0.57	6.1
Zhao et al., 2011 [52]	Mortar	Not specified	16.12	0.760	0.62	7.6
Xie et al., 2007 [46]	Mortar	Screen Printing	12.35	0.694	0.68	5.81

Table 1.1: Comparison of P25-based DSC performances in the literature. Note that the top two performing DSCs included $TiCl_4$ treatments, scattering layers, and anti-reflective coatings. All DSCs were sensitized using N719 dye and employed I-I_3^--based electrolytes.

Implementing the methods in the literature can be challenging as important de-

tails of the techniques are often not stated explicitly or are left out entirely. Thus the principle objective of this research was to evaluate the different paste fabrication, device assembly, and testing techniques for their effect on DSC performance. Specifically, finding methods for making a screen printing paste and assembling DSCs that would yield reproducible device efficiency of ∼6% from commercially available materials was a major goal of this work.

Given the above goals, the scope of this thesis covers the following issues in DSC fabrication. DSCs sealed by thermoplastic gasket or epoxy are compared for performance with each other and unsealed cells. The effect of paste formulation procedure on aggregate size distribution and in turn on film cracking and performance is investigated. A commercial electrolyte and an electrolyte formulated by our lab are evaluated for their effect on DSC performance and their charge transport/transfer properties. Doctor bladed and screen printed films are compared for their uniformity of thickness and performance. Finally, the effect of exposing the dye solution to low pressure during dye loading of DSC films is evaluated.

Chapter 2

EXPERIMENTAL

2.1 Materials

Two different TiO_2 nanoparticles were used to make the photoanodes of the DSCs in this research: commercially available P25 Aeroxide® (Evonik) and nanoparticles synthesized in our lab (hereafter referred to as lab nanoparticles). Commonly used in DSC studies, P25 is manufactured through fumed $TiCl_4$ synthesis. The resulting P25 nanoparticles are a mixture of the anatase (80%) and rutile (20%) phases with diameters of 21 nm and 50 nm for particles of each phase respectively [22]. Figure 2.1 shows the powder x-ray diffraction (XRD) spectra for P25 and the lab nanoparticles with the prominent anatase and rutile peaks labeled. Calculation of the weight fractions of anatase and rutile in the P25 using the method of Spurr and Myers [41] yielded 81% and 19% respectively, in excellent agreement with the published values cited above. The lab nanoparticles are created from a titanium isopropoxide precursor via hydrothermal growth and have an average diameter of 20 nm [53]. As can be seen in the XRD spectrum, the lab nanoparticles are essentially 100% anatase.

The TiO_2 nanoparticles were dispersed in a paste for screen printing or doctor blading. The paste recipe was based on formulations reported by Ito and others [22, 25]. The pastes used a 50/50 mixture of two types of ethyl cellulose (Aldrich 46070 and 46080) as a binder and terpineol (anhydrous, mixed isomers, Aldrich 86480) as the dispersant. The ethyl cellulose was dissolved in ethanol in a 10 wt% solution prior to use in the pastes. Acetic acid was used in the paste to help maintain dispersion of the nanoparticles. The paste formulation and fabrication are described in further detail below.

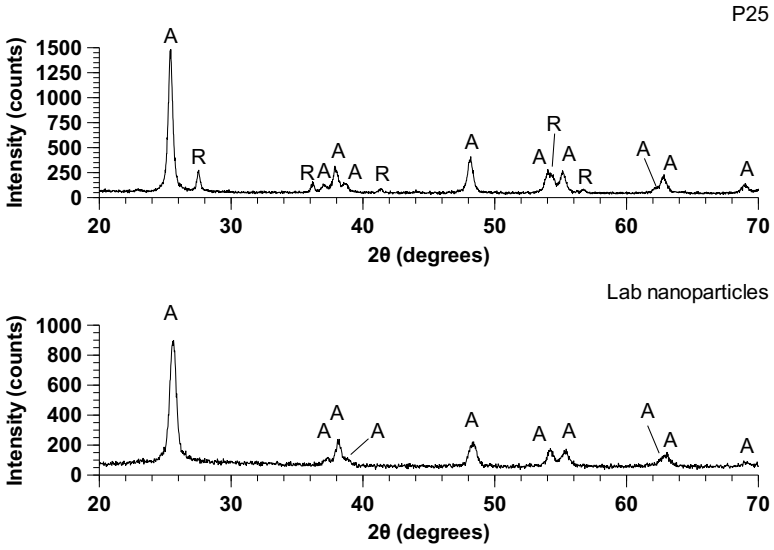

Figure 2.1: Powder XRD spectra for P25 (top) and lab nanoparticles (bottom) with prominent anatase (A) and rutile (R) peaks labeled.

Two different electrolytes were used in the DSCs: a commercial electrolyte (Dyesol's High Performance Electrolyte, MS005615) and an electrolyte formulated in our lab. Both electrolytes are based on the iodide/triiodide redox couple and use acetonitrile and valeronitrile as the solvents. The two electrolytes will be referred to hereafter as the Dyesol HPE and the lab electrolyte respectively, and are compared in performance later in this thesis.

The remaining materials comprising the cells are as follows:

- Photoanode substrate - 2.2 mm-thick TEC 8 ($\sim$8 $\Omega/\square$) and 3.2 mm-thick TEC 7 ($\sim$7 $\Omega/\square$) FTO glass (Pilkington)

- Cathode - 3.2 mm-thick TEC 15 ($\sim$15 $\Omega/\square$) FTO glass coated with a mesoporous platinum film (Dyesol MS001650)

- Spacer and sealing thermoplastic film - 30 μm Surlyn® film (Dyesol MS004610)

- N719 dye (Dyesol MS003190)
- Torr Seal® Epoxy (Varian)

2.2 Methods

2.2.1 Paste Fabrication

Two different paste making methods were investigated in order to determine which method yielded the best and most reproducible DSC performance. The methods differed in the primary technique used to disaggregate the TiO_2 nanoparticles: mortar grinding and ball milling. Both techniques were developed by Ito and others [22, 25], the mortar technique especially being widely cited in the literature. Originally developed for large batch sizes using 6 g of TiO_2 powder, the two methods were scaled for smaller batch sizes of 1.2 to 4.8 g of TiO_2 powder. The paste preparation process for both methods for a 2.4 g TiO_2 powder batch size is shown in Figure 2.2. The mortar method as given in Ito and others [22] included a final roller mill step. P25 pastes were prepared both with and without the roller mill step to assess the affect of the roller mill on final particle size distribution and paste performance. The ball milling technique was tried using both water and ethanol as the milling liquid. Aluminum and iron contamination of DSCs has been found to reduce DSC performance [22, 50], so all paste preparation and DSC assembly were carried out using glass or plastic equipment. Equipment used in the two paste preparation techniques was as follows:

- Mortar - 10 cm diameter, agate
- Probe sonicator - Fisher Sonic Dismembrator 550, 0.5 inch diameter replaceable flat tip, 550 watt maximum output
- Grinding media - Glen Mills, 0.1 - 0.2 mm diameter zirconia beads

- Ball mill - Lortone Rotary Tumbler, Model 33B
- Rotary evaporator - Buchi Rotovapor® RII
- Roller mill - Exakt 50 outfitted with alumina rollers and plastic scraper

2.2.2 Working Electrode Fabrication

Methods to deposit TiO_2 films on the order of 10s of microns thick include dip coating, spin coating, spray coating, doctor blading, and screen printing. Of these methods, screen printing is especially well suited to the roll-to-roll mass production techniques that are hoped to be applicable to DSCs. Screen printing, however, is an involved multi-step process, and for films used for quick, preliminary tests on a lab scale, the doctor blading technique is easier to employ. Doctor blading and screen printing can use the same pastes, while dip coating, spin coating, and spray coating require lower viscosity dispersions of TiO_2 nanoparticles. This thesis focuses on the doctor blade and screen printing techniques, and compares the uniformity and quality of the resulting films.

Before deposition of the TiO_2 film on the FTO substrate by doctor blading or screen printing, all substrates were cleaned using the following procedure:

1. Bath sonicate for 10 minutes in 1 vol% Micro-90 detergent in tap water, rinse under running tap water, rinse with deionized water, dry with lab compressed air.
2. Bath sonicate for 10 minutes in acetone, rinse with acetone, dry with lab compressed air.
3. Bath sonicate for 10 minutes in isopropanol, rinse with isopropanol, dry with lab compressed air.

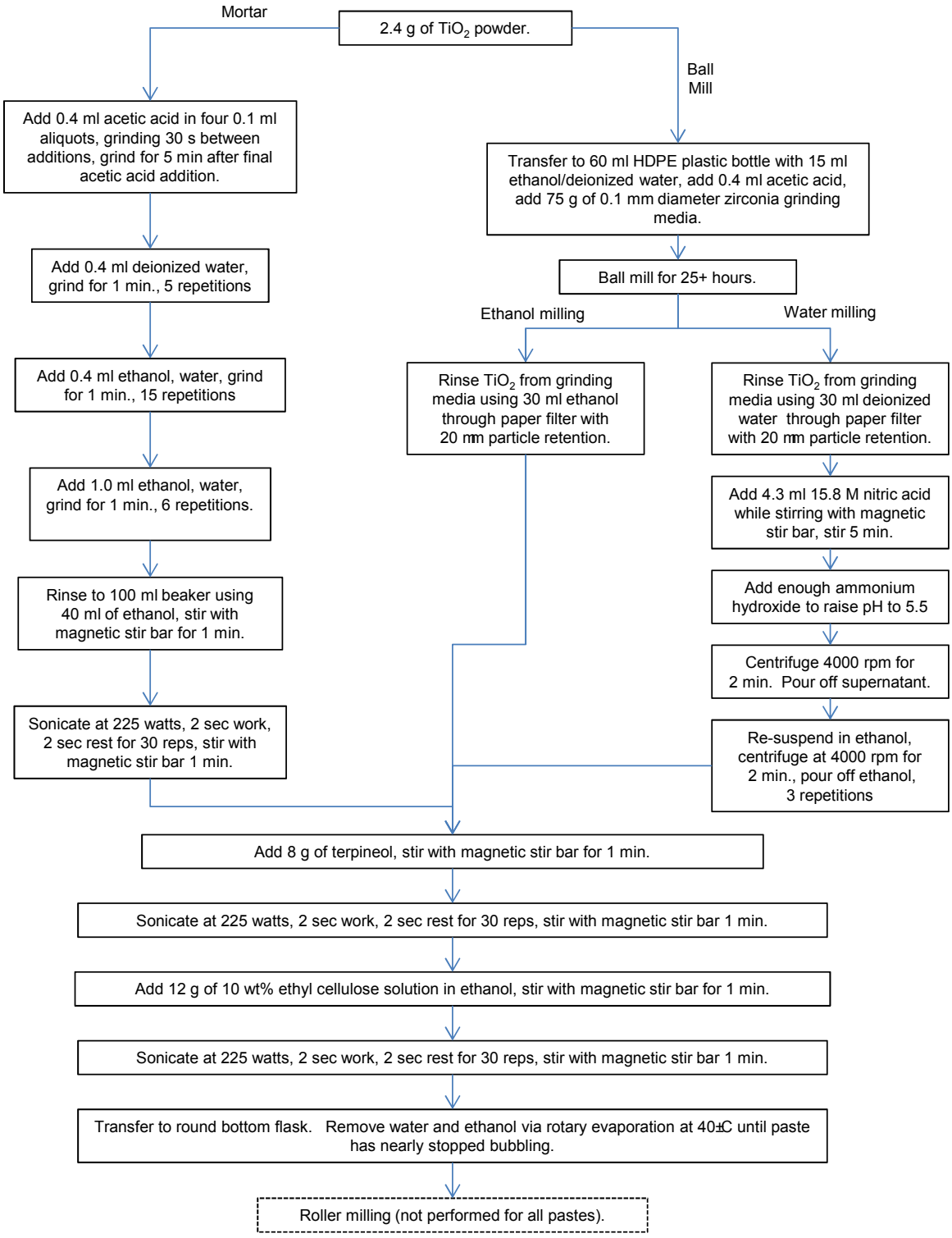

Figure 2.2: TiO_2 paste preparation procedures for mortar and ball milling methods.

If cleaned substrates were not to be used immediately, they would remain submerged in isopropanol until needed, whereupon they would be rinsed with isopropanol and dried with lab compressed air.

Doctor Blade

The doctor blade technique uses a blade to distribute a layer of paste onto the substrate using a scraping motion. Objects commonly used as blades include microscope slides, glass stir rods, and razor blades, as well as blades created especially for this purpose. In this work, a microscope slide was used as a doctor blade to avoid metal contamination of the paste. One layer of Scotch® tape with a thickness of approximately 53 μm was used as a spacer between the substrate and the blade to create the desired paste thickness. With the minimum paste thickness dictated by the thickness of a single layer of tape, the doctor blade technique offers limited control of the paste layer thickness.

Screen Printing

Screen printing is a widely used technique to deposit pastes on a substrate, particularly in the electronics industry where it is used to create traces and lettering on printed circuit boards. The basic equipment required is a mesh screen, and a squeegee to press the screen onto the substrate and force the paste through the screen onto the substrate. The screen is coated with an emulsion to block paste from moving through the screen except in the areas where paste deposition is desired.

The thickness and quality of a screen printed film depends on a great number of factors including the screen mesh thread spacing, mesh thread diameter, squeegee angle, squeegee speed, squeegee pressure, paste viscosity, and snapoff distance [37]. Due to the great number of factors that need to be controlled, repeatable screen printing results are best obtained by using a screen printing machine. For research purposes, however, screen printing can be done by hand as was done in this thesis.

The screen used to make the films were manufactured by SEFAR, Inc. Screens were constructed of polyester mesh coated with SEFAR's E80 emulsion. The E80 emulsion was chosen for its durability and resistance to a wide range of solvents. Two different meshes were used. To deposit a roughly 2.5 μm-thick film (post-calcination), a 230 thread per inch (TPI) mesh with 48 μm diameter threads was used. To deposit a roughly 5 μm-thick film (post-calcination), a 110 thread per inch (TPI) mesh with 80 μm diameter threads was used. Both meshes were mounted on 8 inch by 10 inch aluminum frames. The screen printing station was set up so that the separation between the substrate and the screen (e.g. the snapoff distance) was 2 mm. The screen printing station is shown without and with the 110 TPI mesh screen in Figures 2.3a and 2.3b respectively.

(a) Screen printing station without the screen. Pieces of FTO glass the same thickness as the substrate to be printed upon are used to keep substrates in the same position when multiple layers are printed.

(b) Screen printing station with the 110 TPI screen. Aluminum posts adhered to the glass station base allow consistent positioning of the screen.

Figure 2.3: Screen printing station.

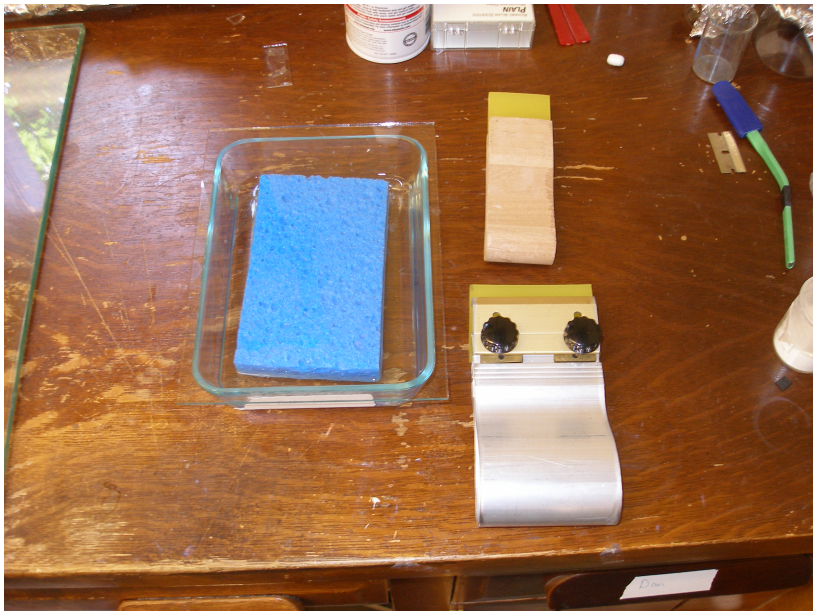

Figure 2.4: Metal and wood handle squeegees (right) and relaxation chamber (left).

The squeegee used to perform the screen printing was a 3/8 inch wide, urethane, durometer 70 squeegee with a square profile held in a wooden or metal handle as shown in Figure 2.4. The metal handle was adopted for later films due to occasional flaking of wood fibers into the paste. The metal handle also helps prevent the squeegee from bending along its length during printing. The squeegee was held at an approximately 45° angle during printing.

The relaxation chamber used to smooth the film surface and reduce the screen mesh marks between printing layers consisted of a ethanol-soaked sponge in a glass container as shown in Figure 2.4. Relaxation times needed to achieve a smooth surface varied with paste viscosity, with more viscous pastes taking long to relax. The relaxation time for all pastes increased with number of layers printed. Typically, the first printed layer would take 1 to 3 minutes to relax. The second printed layer would take 3 to 10 minutes to relax. The third layer could take upwards of 15 minutes to relax for some particularly viscous pastes. During relaxation, the film

edges would thicken substantially, so film areas larger than the desired final 5 mm by 5 mm film were printed and the excess film scraped away after calcination using a glass microscope slide.

The screen printing procedure was adapted from Ito and others [22] as follows:

1. Secure substrate to printing base using double-sided tape. Used spray duster to remove dust from substrate surface.

2. Using squeegee, load paste onto screen until paste is visible coming through the mesh on the emulsion side of the screen.

3. Placing screen over substrate, use squeegee to press screen onto substrate and slide squeegee across substrate depositing the film.

4. Remove substrate and immediately place into relaxation chamber to allow paste surface to smooth. Immediate placement of substrate into relaxation chamber after printing is important. Unrelaxed films left to sit before being placed in the chamber will become more viscous and take longer to relax.

5. Dry film in 125°C oven for 6 min.

6. Repeat steps 1-5 until desired film thickness is achieved.

2.2.3 Cell Assembly

After printing/doctor blading and drying the film, the film was calcined in a furnace. Calcination temperature profiles for DSC TiO_2 films vary in the literature. Some procedures involve several dwell steps at intermediate temperatures along the path to the maximum temperature [22], while other profiles go straight to the maximum temperature [50]. One of the focuses of this research was to reduce cracking in the film that occurs during calcination. Both stepped and monotonic temperature profiles

were tried, and neither seemed to reduce cracking of the films. As DSC performance with η above 8% has been reported in the literature with both types of calcination temperature profiles [22, 50, 25], a simple monotonic temperature profile with a ramp rate of 5°C/min to 500°C, a dwell time of 30 minutes at 500°C, and a step to room temperature at the natural cooling rate was adopted for this research.

If the cells were to be tested in a sealed configuration, then the platinum-coated counter electrodes had to be drilled before assembly to create a 1 mm diameter hole for vacuum-assisted electrolyte infiltration after assembly. To drill the holes, a 1 mm diameter, diamond-coated bit (Lasco Diamond Products, Inc.) was used in a Dremel® 4000 rotary tool set at 20,000 rotations per minute (rpm). To extend the diamond bit life and eliminate glass dust generation, the counter electrode was submerged in deionized water during drilling. The cathode was placed on a microscope slide to provide support during drilling. The hole was started on the platinum-coated side of the electrode due to fracturing that would enlarge the hole size as the bit exited the backside of the electrode. After drilling the hole, the counter electrode would be rinsed with deionized water and ethanol, and dried with the lab compressed air.

After calcination and cooling to room temperature, the TiO_2 films would be re-heated to approximately 80°C for 30 minutes to drive off adsorbed water from the film surface. The heated film would then be placed into a glass container, immersed in a 0.5 mM N719 dye ethanol solution, and covered with Parafilm®. After 24 hours of dye loading, the substrates would be removed from the dye solution, rinsed with ethanol, immersed for several seconds in ethanol, and dried with the lab compressed air. Ideally, the substrates would be immediately tested if the open cell testing configuration was to be used, or the cell would be assembled, sealed, and infiltrated with electrolyte. Sealed cells were either tested within an hour of electrolyte infiltration or stored in a dark drawer overnight and tested the following day. If cells could not be sealed and/or tested immediately after completion of dye loading, they would be placed in polycarbonate petri dishes wrapped in foil and stored under vacuum until

Figure 2.5: Smoothing gasket onto the substrate with stir rod. Smoothing gasket helps achieve rapid sealing without gaps in the seal.

assembly and testing were possible. Storage under these conditions for more than a few days, however, would lead to large decreases in cell V_{oc}, J_{sc}, and η.

Two different methods were investigated for sealing DSCs. In one method, a thermoplastic Surlyn® film gasket served as both a spacer and sealant. The gaskets were 13 mm by 13 mm square with 2 mm-wide walls. To seal the cell, the gasket was placed on the FTO side of the photoanode. To ensure that the gasket lay flat on the substrate so that the cell would seal quickly and effectively, the gasket would be smoothed onto the substrate by rolling a piece of glass stir rod firmly across the gasket as shown in Figure 2.5. The cathode was then placed Pt film side down over the photoanode, aligned so that the hole would not be over the TiO_2 film.

Hot sealing was performed in a Specac hydraulic press with Specac 6100+ heated platen controller as shown in Figure 2.6a. The first hot sealing procedure used was to place the DSC in a hot platen press with top and bottom platens heated to 100°C and compress the DSC under 1.5 kN of force for 45 seconds. This was the hot sealing procedure used to compare hot sealed, epoxy sealed, and unsealed DSC configurations.

While this configuration would seal the DSC, it would often cause excessive and uneven spreading of the gasket because the top platen was free to tilt. To address this issue, the top platen was removed from the press and the bottom platen was heated to 120°C as shown in Figure 2.6b and exposed to 2.0 kN of force for 30 seconds. To prevent excessive conduction of heat from the working electrode into the unheated top platen of the press, a 2.2 mm thick piece of glass was placed on the working electrode. This press configuration would produce good sealing of the DSC without excessive spreading of the gasket material.

For the epoxy sealing method, the thermoplastic gasket served only as a spacer to set the cell gap. Positioning of the gasket was identical to the heat sealing procedure. Once the cathode was in place, the cell would be held together with binder clips and epoxy placed along the gap edge of the cell. Capillary forces were then sufficient to draw epoxy into the cell gap, effectively sealing the cell as shown in Figure 2.7. Two epoxies were tried: a solvent-based, 5-minute epoxy (Devcon 5-minute epoxy) and a solvent-free epoxy designed for high vacuum applications. The 5-minute epoxy was found to interact with the solvent in the electrolyte and degrade DSC performance, so the solvent-free epoxy was used for DSC sealing and testing. The solvent-free epoxy was allowed to cure for 24 hours at room temperature prior to electrolyte infiltration.

To infiltrate the electrolyte and complete sealing of the DSC, the DSC was placed in a vacuum chamber counter electrode side up. A small piece of glass tubing was placed over the hole as shown in Figure 2.8 and three drops of electrolyte were placed in the tubing. The vacuum chamber was then evacuated until bubbles stopped emerging from the hole in the DSC while trying to avoid boiling the electrolyte excessively (boiling occurred at approximately 150 mbar pressure). Air was then slowly reintroduced to the vacuum chamber, forcing electrolyte into the cell gap. If bubbles remained in the cell gap, the process was repeated until no bubbles were visible.

After electrolyte infiltration, excess electrolyte was cleaned from the DSC surface using an ethanol dampened tissue. An 8 mm by 8 mm square of thermoplastic film

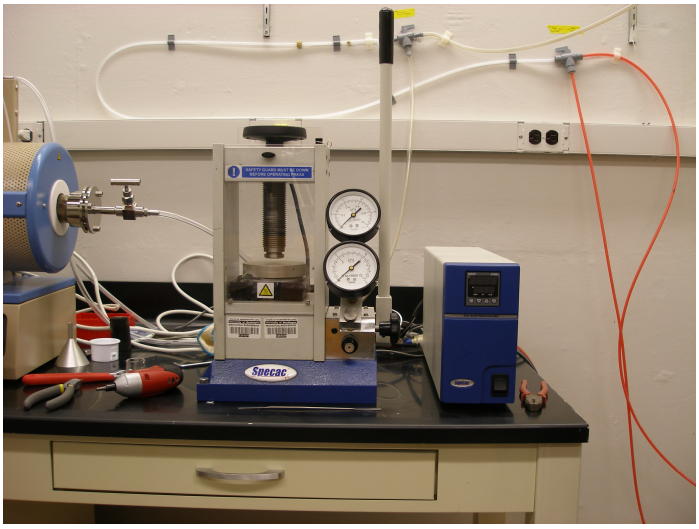

(a) Press and heated platen controller.

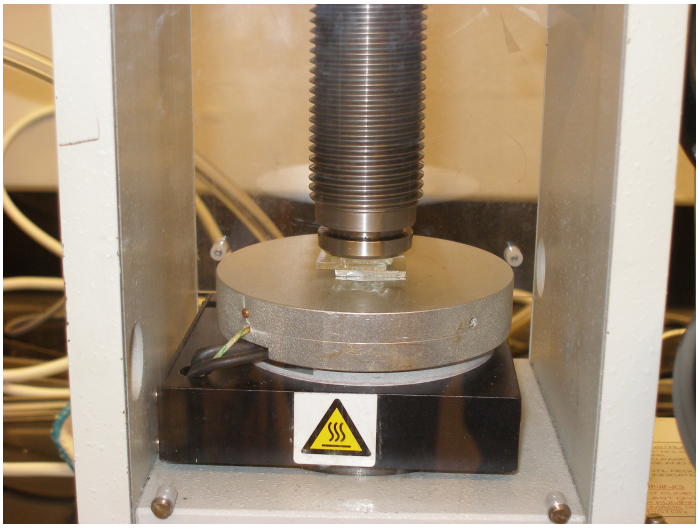

(b) Press with bottom heated platen but not the top heated platen. Cell to be sealed and extra 2.2 mm-thick glass for insulating the top platen from the cell in place.

Figure 2.6: Setup of hot platen press for DSC sealing with thermoplastic gasket.

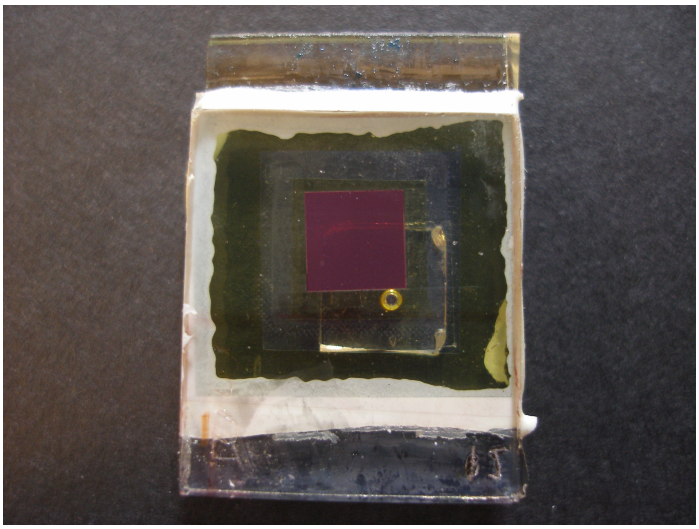

Figure 2.7: Epoxy-sealed DSC. Epoxy pulled into the cell gap by capillary forces can be seen at the edges of the cell.

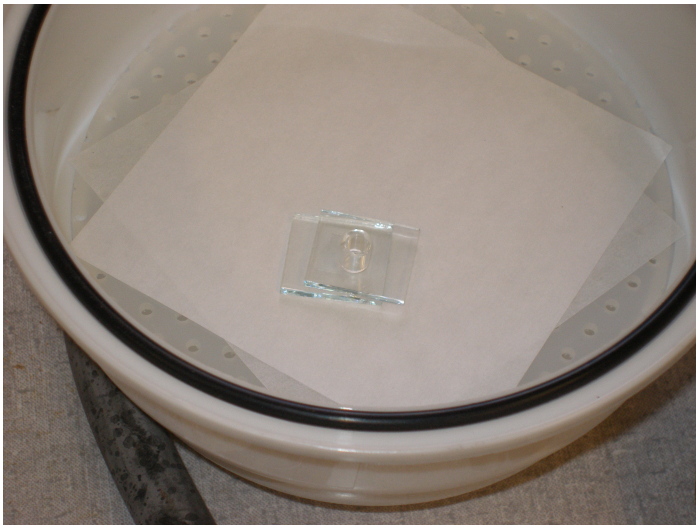

Figure 2.8: Cell in vacuum chamber for electrolyte infiltration with glass tubing positioned over infiltration hole to hold electrolyte.

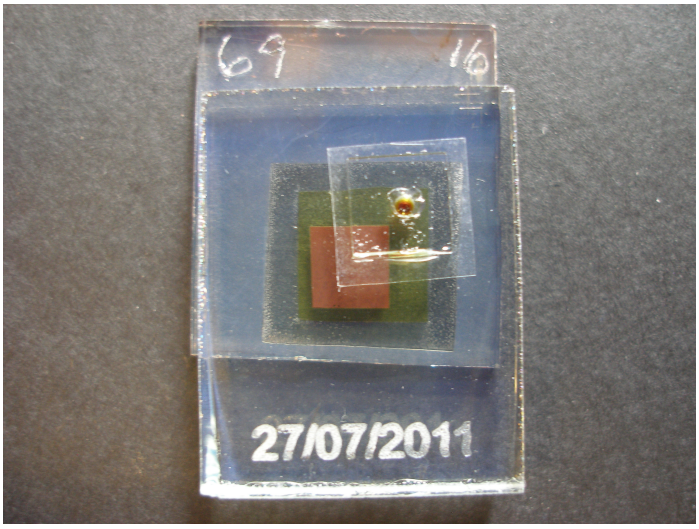

Figure 2.9: Back of sealed DSC showing Surlyn® film and glass cover over electrolyte infiltration hole.

(i.e. the film cut from the center of the gasket) was placed over the hole and pressed into place with finger pressure. A 6 mm by 6 mm piece of microscope slide that had been heated on a hotplate set at maximum temperature was then pressed onto the film over the hole and held in place for 10 seconds. The back of the sealed DSC is shown in Figure 2.9.

2.3 DSC Characterization

2.3.1 J-V Curves

The J-V characteristics of the DSCs were measured using an Oriel xenon lamp, Newport 67005 lamp housing, Newport 69907 power supply, Keithley 2400 sourcemeter, and Keithley LabTracer software. The light beam was passed through an AM1.5 filter, and the intensity of the light at the location of the DSC was calibrated to 100 mA/c^2m using a Hamamatsu monocrystalline photodiode of area 0.076 cm^2 that had be itself calibrated at the National Renewable Energy Lab.

The light source used in these experiments is not uniform, with the intensity of the light beam at a maximum near the center of the beam and diminishing toward the edges. As a result of light source inhomogeneity, other researchers have shown that placement of the DSC within the light beam in the same position as the calibration photodiode and orientation of the DSC perpendicular to the light beam are critical to getting accurate, repeatable measurements [40]. Accordingly, the DSC was placed on a mount as shown in Figure 2.10a that would place the DSC the same distance from the light source as the calibration photodiode and assure a perpendicular orientation to the light beam as shown in Figure 2.10b. The DSC mount also has a black background to prevent reflected light from the mount from erroneously boosting DSC performance. The DSC was aligned within the beam of light by collimating the light beam with a pin hole and aligning the DSC so that the pinpoint of light fell on the approximate center of the TiO_2 film as shown in Figure 2.10c.

Initially, the LabTracer software was setup to run with without signal integration or a time delay between samples. An unusual current density spike around 4 mA/cm^2 appeared in all of the J-V curves. While the source of the noise was not determined, it was found that the spike could be removed by integrating the measurement signal over 1 power line cycle (e.g. 1/60 sec) and setting the sample time delay to 3 ms. These measurement settings were used for all J-V data collection except for the comparison of heat sealed, epoxy sealed, and unsealed cells.

When testing unsealed cells, the DSC would be assembled in the mount with two narrow strips of weigh paper as spacers as shown in Figure 2.11. After attaching measurement electrodes to the cell, a drop of electrolyte would be place on the unsealed cell gap on the counter electrode and drawn into the cell by capillary action. The DSC would be quickly mounted on the light source, aligned within the beam using the collimated light beam, and tested to avoid excessive loss of electrolyte during testing.

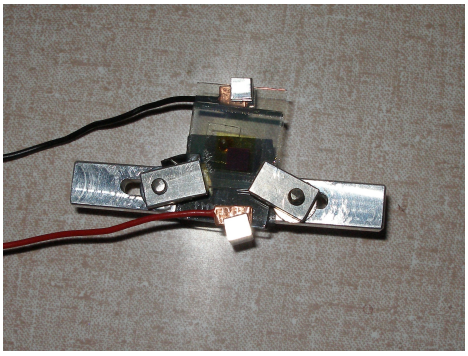

(a) Sealed DSC in the testing mount.

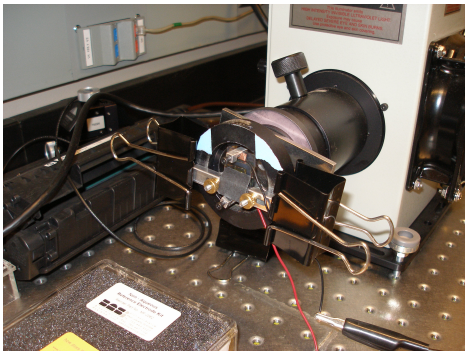

(b) DSC in position.

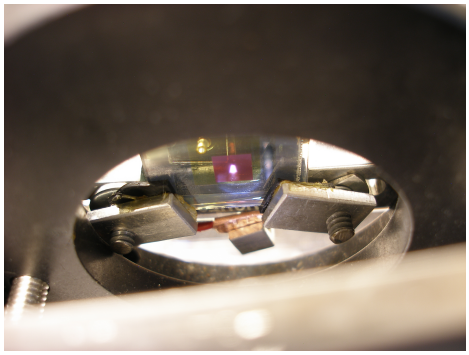

(c) DSC positioned with collimated light beam in the approximate center of the TiO_2 film.

Figure 2.10: DSC mounting for J-V testing.

2.3.2 Electrochemical Impedance Spectroscopy

Charge movement within the DSC plays an important role in determining a DSC's performance and can be subdivided by location. The locations at which charge transport takes place are within the FTO layers on the photoanode and cathode, within the TiO_2 film, and within the electrolyte. The locations of charge transfer are at the electrolyte-platinum film interface at the cathode, at the electrolyte-TiO_2 film interface, photoanode FTO layer-TiO_2 film interface, and at the photoanode FTO

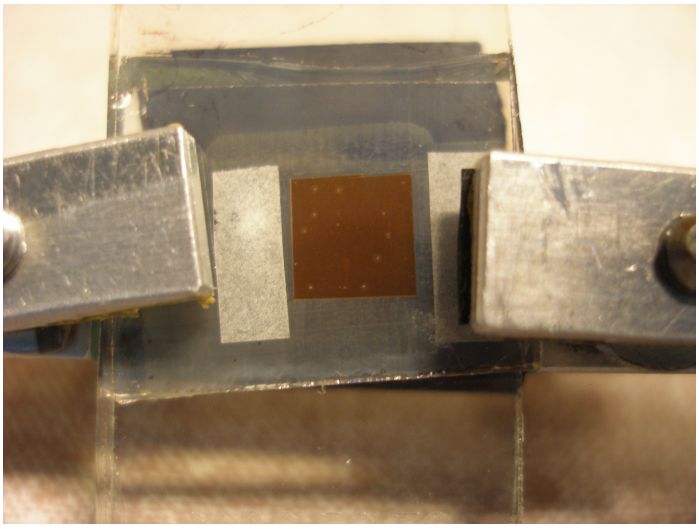

Figure 2.11: DSC in mount with weigh paper spacer for open testing.

layer-electrolyte interface.

The charge movement mechanisms within the TiO_2 film, at the TiO_2 film-electrolyte interface, and within the electrolyte are very different. Due to the charge screening effects of ions within the electrolyte and the nanoscale crystallite size, electric fields within the TiO_2 film are so small that charge transport occurs primarily through diffusion [12, 15, 16]. Under illuminated conditions, charge transfer at the TiO_2 film-electrolyte interface occurs through reduction of the oxidized dye molecule by I^-, and by reduction of I_3^- by electrons from the TiO_2 conduction band. The latter of the two TiO_2 film-electrolyte reactions is the main recombination reaction that reduces the performance of the DSC. Charge transport within the electrolyte occurs through diffusion of the I^-/I_3^- species within the electrolyte.

These charge transport and transfer mechanisms can be characterized by electrochemical impedance spectroscopy (EIS). In EIS, the impedance of the DSC is calculated from the current response of the DSC to a small amplitude, oscillating voltage. The oscillating voltage frequency is scanned over a set range while a direct

current voltage bias is applied to the DSC. By modeling the DSC as an equivalent circuit of various circuit elements, the resistance associated with a particular charge transport or transfer mechanism can be determined.

EIS was used to measure the charge transfer resistance at the electrolyte-TiO_2 ($R_{ct\text{-}TiO_2}$) and electrolyte-Pt film ($R_{ct\text{-}Pt}$) interfaces, as well as the diffusion coefficient ($D_{I_3^-}$) for I_3^- for three different electrolytes; the lab electrolyte and two different batches of the Dyesol HPE that were received and opened at different times. Cells consisting of TiO_2-Pt and Pt-Pt electrode combinations were tested. As shown below, $D_{I_3^-}$ does not show up well in the dark-tested TiO_2-Pt cell, but is easily seen on the Pt-Pt cell.

Impedance spectra were collected using a Solartron SI1287 electrochemical interface (potentiostat) and Solartron SI1260 impedance/gain-phase analyzer. Cells were measured under dark conditions to avoid photochemical induced changes in the I_3^- concentration in the electrolyte. The voltage bias was -0.75 V for the TiO_2-Pt cells, the bias chosen to accentuate the electrolyte-Pt interface response on the Nyquist plot. The accentuation occurs because the higher bias raises the Fermi level in the TiO_2 film, thus making the charge transport resistance R_d within the film much smaller than $R_{ct\text{-}TiO_2}$ and in turn causing the curve associated with the electrolyte-TiO_2 interface to take an more pronounced semicircular shape [9]. The bias on the Pt-Pt cell was set to 0 V because higher voltages created excessive noise in the impedance data. The frequency range scanned was 10^5 to 0.1 Hz. Since the impedance involving the electrolyte depends on the surface area of the TiO_2 film-electrolyte interface, EIS results between films of similar thickness and printed area were compared. Since film porosity may be different for different pastes thus affecting the TiO_2 film-electrolyte interface area, films for EIS comparisons were made with the same paste.

2.3.3 Film Area and Thickness Measurements

Because DSC performance depends so strongly on the TiO_2 film area and thickness, it is important to measure those parameters of the TiO_2 film to allow accurate comparisons of DSC performance among different films. Furthermore, the film area and thickness are used in calculating performance parameters of the cell. For example, film area is used to calculate current density (J), while film thickness is used to find the effective diffusion coefficient of electrons within the film [1]. Consequently, film area and thickness were measured for all of the films in this study.

Film thickness measurement were made with a Sloan Dektak 3030, Tencor Instruments Alpha-step 500, or Tencor Instruments P-15 contact profilometer. Profile measurements of different doctor blade techniques where film thickness was recorded and graphed were made on the P15. All other measurements were made on the Dektak or Alpha-step. Mesoporous TiO_2 films are easily scratched, so the tip force was set between 1 mg and 5 mg. Scan lengths were 2 mm on the Alpha-step and 8 mm on the Dektak. Scan lengths were limited to 2 mm on the Alpha-step as longer scans did not give accurate results due to leveling problems with the instrument. Since film dimensions were approximately 5 mm by 5 mm, the Dektak scans could give a profile across the entire surface of the film.

DSC researchers often calculate the area of rectangular active layer films by measuring the lengths of the sides of the film using digital calipers and multiplying the lengths together. Ito and others [24] showed that this measurement technique may lead to errors in the DSC film area calculation. These errors can be attributed to either difficulty in aligning the caliper jaws with the edges of the film or in deviation of the film area from a rectangular shape. The later is particularly a problem when the film is created by scraping away portions of a larger film to remove thickened areas at the film edges as was done in this study. Consequently, film areas in this study were measured using scanning procedure [24].

To measure the film areas, the photoanodes were placed film side down on a standard office scanner. The films were then scanned at 1000 dots per inch (dpi) resolution against a black background resulting in a grayscale image of the film as shown in Figure 2.12a. The image was then processed with a Sobel filter to create an "elevation" map of the image that highlights the film edges as shown in Figure 2.12b. The film area was then calculated by applying a watershed segmentation algorithm to the "elevation" map [5] resulting in the delineated film area shown in Figure 2.12c. Image processing was performed in Python using the Scikits-image module. For substrates for which the algorithm failed, the edges of the film were outlined manually in image processing software.

As shown in Table 2.1 below, the coefficient of variation for quantities calculated using the film area (e.g. J_{sc} and η) for films made from the same TiO_2 paste is reduced when the scanned film areas are used versus film areas calculated from film dimension caliper measurements. Even though the coefficient of variation for the areas themselves is relatively small, the error in the film area measurement propagates through the J_{sc} and η calculations, increasing the coefficient of variation for those quantities. Note that the fill factor does not depend on the film area as the film area cancels out of the fill factor calculation.

2.3.4 Dynamic Light scattering

Particle size distributions in the pastes were characterized using dynamic light scattering (DLS). Samples of paste were dispersed in ethanol and sonicated for 1 minute. The particle size distribution was measured using a Zetasizer DLS (Malvern Instruments).

Scanning electron microscope (SEM) images were collected with a JEOS JSM-7000 field emission SEM.

Ultraviolet-visible (UV-vis) transmittance and diffuse reflectance spectra were collected with an Evolution 300 UV-vis spectrophotometer (Thermoscientific). A DSA-

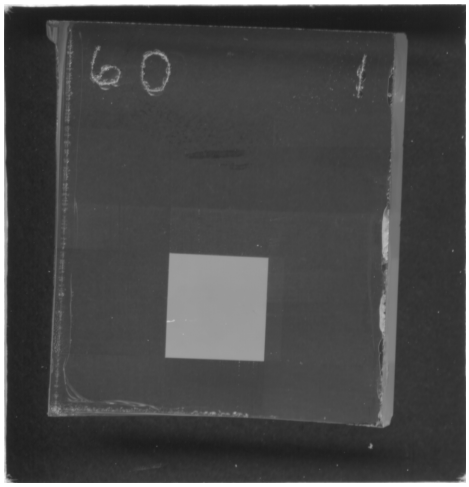

(a) 1000 dpi grayscale scan of undyed TiO_2 film.

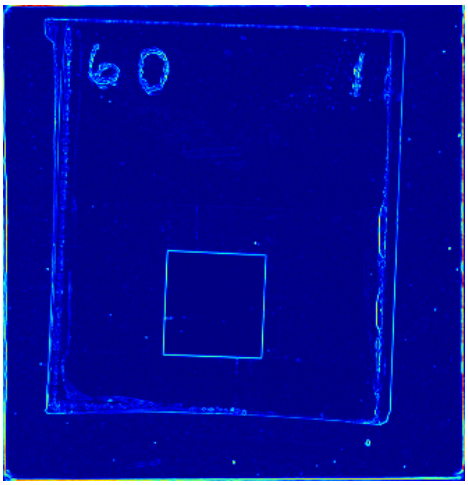

(b) Sobel filter "elevation" map of grayscale image.

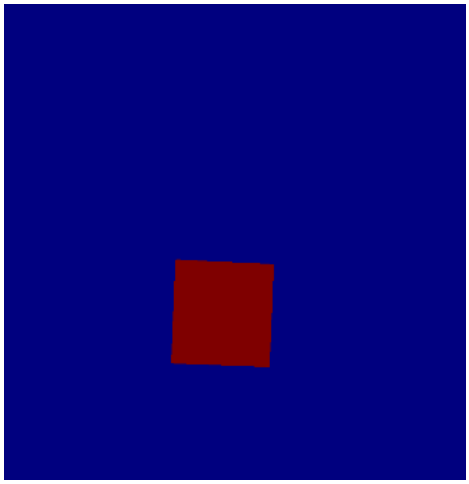

(c) Delineated TiO_2 film area resulting from application of watershed segmentation algorithm to "elevation" map.

Figure 2.12: Image processing of scanned TiO_2 film to measure film area.

Sample	Digital Caliper Measured			Scanned		
	Film Area (cm^2)	J_{sc} (mA/cm^2)	Efficiency (%)	Film Area (cm^2)	J_{sc} (mA/cm^2)	Efficiency (%)
b60s05	0.362	7.97	4.13	0.346	8.34	4.32
b60s06	0.351	8.88	4.54	0.356	8.75	4.47
b60s07	0.315	7.92	4.08	0.311	8.02	4.14
b60s08	0.358	8.25	4.15	0.342	8.64	4.34
Average	0.347	8.26	4.22	0.339	8.44	4.32
Coefficient of Variation (%)	6.2	5.4	5.0	5.7	3.9	3.2

Table 2.1: Effect of TiO_2 film area measurement method on DSC performance measures.

EV 300 diffuse reflectance accesory with a Spectralon® reference was used to collect diffuse reflectance spectra. All spectra were collected with the TiO_2 film wetted with acetonitrile and covered with a glass coverslip.

Chapter 3
RESULTS AND CONCLUSIONS

DSC performance depends significantly on the materials used in the cell and the fabrication techniques used to assemble the cell. Unlike the early days of DSC research when most DSC materials were made in-house, pre-made DSC materials such as TiO_2 screen printing pastes, electrolytes, dyes, and counter electrodes may be purchased from commercial vendors. Furthermore, a variety of techniques may be used to assemble and test DSCs. This section investigates the effects of different TiO_2 screen printing pastes, electrolytes, and assembly techniques on DSC performance.

3.1 Influences of Film Structure

3.1.1 Paste Preparation Methods

The TiO_2 film on the photoanode serves many critical functions within a DSC. The film provides a high surface area for dye loading and charge transport of excited electrons to the FTO layer on the substrate. The network of pores within the film allows I^- ions to reduce oxidized dye molecules, and provides a route out of the film for I_3^- ions diffusing to the cathode to be reduced. Thus the quality of the TiO_2 film has a direct bearing on the performance of the DSC.

The overall properties of the TiO_2 film depends both on the characteristics of the individual nanoparticles and physical characteristics of the film as a whole. Examples of the former include nanoparticle size, phase, crystallinity, and internal structure. Examples of the latter include the porosity of the film, the film surface area, the presence of nanoparticle aggregates and/or agglomerates, the connectedness of adjacent nanoparticles, and the adhesion strength of the film to the substrate. In

particular, the effect of the paste making technique on the particle size distribution within the TiO_2 paste and in turn on DSC performance were investigated. In the following discussion on particle size distribution, the term "aggregate" will be used to identify strongly bound nanoparticles, and "agglomerate" for weakly bound particles that form after disaggregation. The term "cluster" will refer generally aggregates or agglomerates as they cannot be distinguished by DLS. "Particle" will refer to the individual nanoparticles comprising the clusters.

The TiO_2 nanoparticles used to make the pastes begin in an aggregated state. The aggregates of P25 form during the fumed $TiCl_4$ synthesis process, whereas the hydrothermally grown lab nanoparticles aggregate when they are removed from suspension and dried. Much of the paste making process involves separating the nanoparticles. Disaggregating the nanoparticles has several advantages. The more disaggregated the nanoparticles in the paste, the higher the particle density in the film and the higher the dye loading [25]. As micron-sized aggregates tend to scatter incoming light, disaggregating nanoparticles to a few tens of nanometers allows light to penetrate further into the film, improving light absorption [22]. Indeed, much of the increase in performance seen in DSCs by adding a scattering layer of large nanoparticles (approximately 200 nm diameter) on the back of the main layer of nanoparticles may be lost if the particles in the main layer are not well disaggregated. Lastly, as will be shown below, aggregates of nanoparticles tend to cause cracking of the film and peeling from the substrate.

Once particles are disaggregated, the challenge becomes preventing them from joining back together to form agglomerates. In the paste formulation used in this research, re-agglomeration is minimized using acetic acid and terpineol. The acetic acid adds hydrogen ions to the surface of the nanoparticles, the resulting positive surface charge creating repulsive forces between particles. The terpineol acts as a dispersant, coating the surface of the nanoparticles and interfering with bonding between the nanoparticles. Even with acetic acid and terpineol, the suspensions are

Paste	Particle	Particle Dispersion Technique			
		Sonication	Mortar	Roller Mill (passes through)	Ball Mill (hours)
PB42a	P25	X	X		
PB42b	P25	X	X	5x	
PB44	P25	X	X	15x	
PB45	Lab	X	X		
PB46	P25	X			25
PB48	P25	X			42

Table 3.1: Dispersion techniques used for pastes.

unstable, with the nanoparticles being observed to agglomerate if allowed to remain in the ethanol sol for several hours before being turned into a paste.

The methods used to disaggregate the nanoparticles in the paste making procedures were mortar grinding, ball milling, roller milling, and sonication. Batches of paste were prepared using both P25 and lab nanoparticles, with pastes getting various combinations of disaggregation methods as summarized in Table 3.1. Figure 3.1 shows the hydrodynamic cluster diameter as a percentage of total particle volume as measured using DLS. Volume fraction is given in the DLS plots instead of intensity or number fraction because the presence of clusters greater than 1 μm in diameter is more apparent on the volume fraction plot. The distributions in Figure 3.1 are for pastes that went through the same mortar grinding and sonication procedures as given in Figure 2.2, but had a different number of passes through the roller mill.

Several conclusions can be drawn from the cluster size distributions in Figure 3.1. The roller mill does not seem to be able to significantly reduce the peak cluster size of the distribution. Paste batches 42a and 42b, which were made by splitting paste batch 42 into two aliquots, have similar peak cluster sizes, despite 42b having been through the roller mill five times and 42a not at all. Paste batch 44, which was prepared using the same mortar grinding and sonication procedure as 42 and went through the

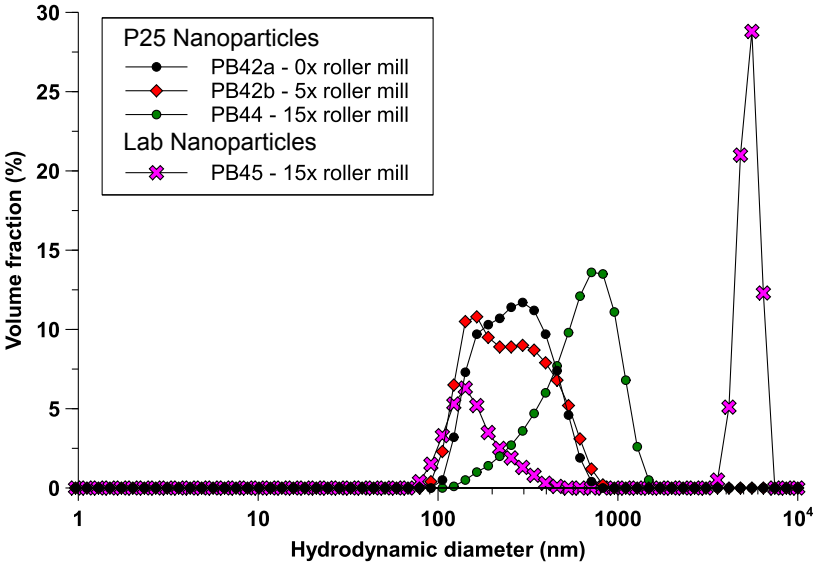

Figure 3.1: Particle size distribution for mortar ground pastes with and without roller milling. The number of passes of the paste through the roller mill is shown (i.e. 0 times, 5 times, and 15 times)

roller mill 15 times, actually has a larger peak cluster size than 42a which did not go through the roller mill at all. Batch 45, which was also made using the same mortar grinding and sonication procedure but used the lab nanoparticles and had 15 passes through the roller mill, had a significant volume fraction peak of clusters larger than 1 μm in diameter. These results indicate that the controlling step on the final cluster size distribution in the paste occurs earlier in the paste making process, either in the mortar grinding or sonication step. Given that the variables in the sonication step are easily controlled, the variability in the final cluster size distribution is likely due to the mortar grinding step. As the mortar grinding is done by hand, this result is not surprising.

Films were screen printed using the pastes in Figure 3.1 two layers thick using the 110 TPI mesh resulting in films around 10 μm thick post-calcination. Optical microscope images of the films are shown in Figure 3.2. The degree of cracking of the

resulting films seems to correlate with the particle size distribution: the larger the clusters and the higher the percentage of the volume fraction of the film, the worse the cracking.

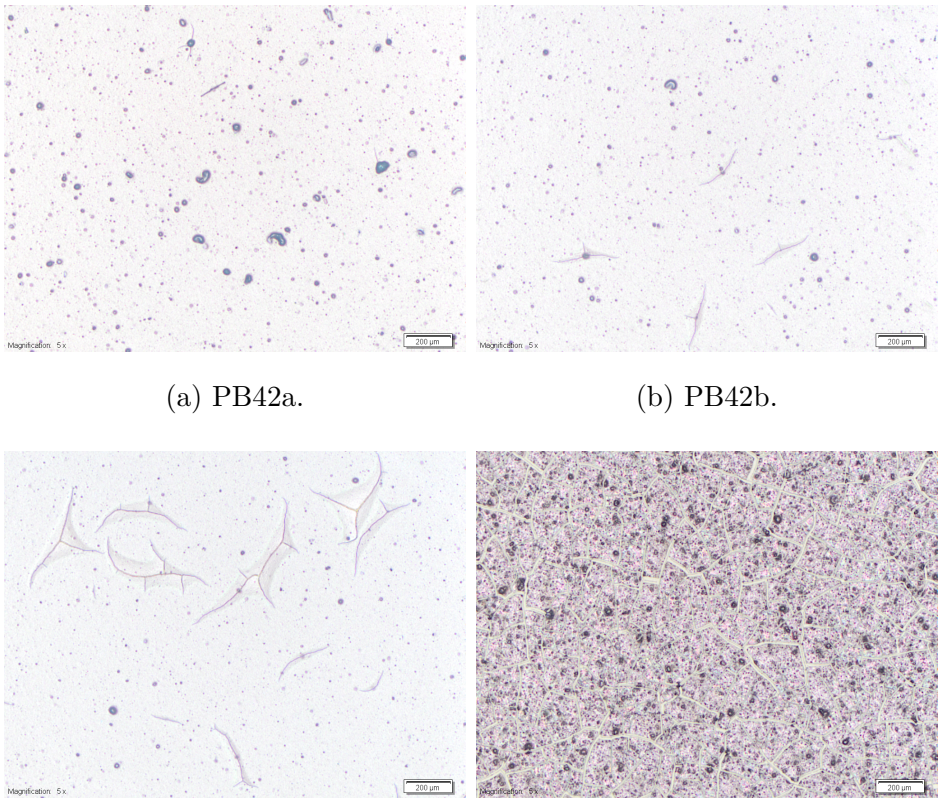

(a) PB42a. (b) PB42b.

(c) PB44. (d) PB45.

Figure 3.2: Optical microscope images of films made from mortar ground and roller milled pastes. Films are not dye loaded.

Cracks seem to nucleate on the large clusters, likely due to the weak bonding between large clusters and the higher stresses around the large clusters. The poor bonding could result from the irregular shape of the clusters. Others researchers have found that when P25 nanoparticles agglomerate in aqueous suspensions, they form irregular particles with fractal geometries [55, 26] as shown in Figure 3.3. When

the film shrinks during calcination, the irregular geometry of the clusters results in poor packing of the clusters, which in turn leads to reduced contact area between adjacent clusters resulting in weak bonding and stress concentration at the bonding site. The irregular clusters would also have reduced contact area with the substrate, again leading to stress concentration and reduced adhesion.

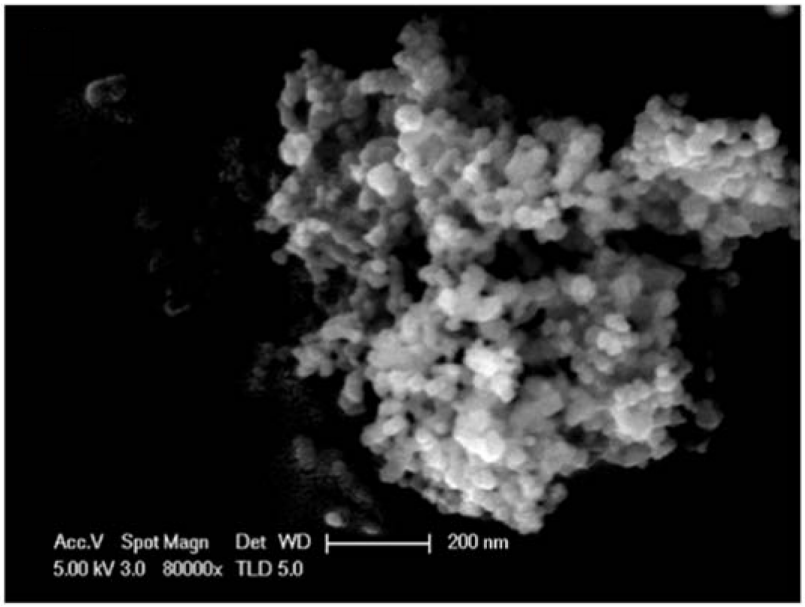

Figure 3.3: Agglomerate of P25 formed in aqueous dispersion from Zhou and others [55].

Ball milling gives much better initial disaggregation of the P25 nanoparticles. As shown in Figure 3.4, a sample taken immediately after 25 hours of ball milling gave a peak cluster size distribution around 60 nm for paste batch PB46. Paste batch PB48 was milled for 42 hours and had a slightly smaller peak cluster size than PB46. The less efficient grinding for PB48 likely resulted from the grinding media charge for PB48 being half that for PB46. Once the dispersions were formulated into pastes, however, the peak cluster size distribution increased to over 100 nm. In the case of PB46, at least some of this re-agglomeration was result of the dispersion being

stirred for two days before being turned into paste. PB48, however, was taken from dispersion to paste within a couple hours of the completion of ball milling, so time for agglomeration was minimized.

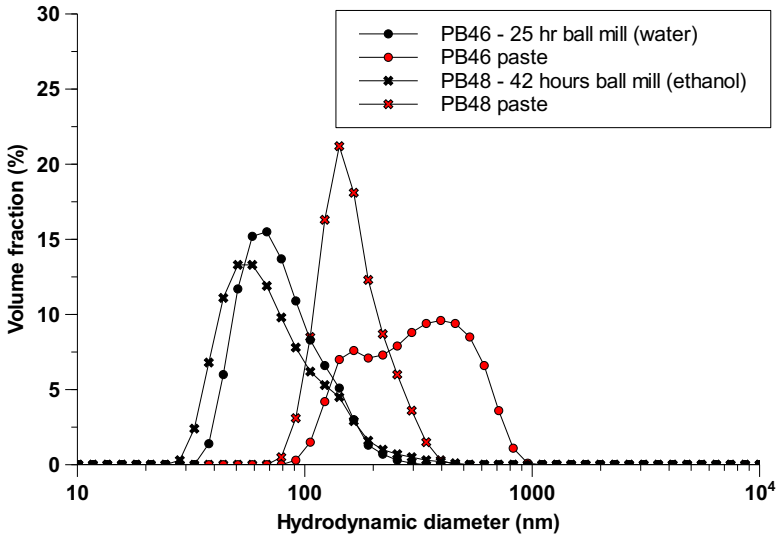

Figure 3.4: Particle size distributions for ball milled P25 pastes both immediately after dispersion (black markers) and after re-dispersion of the particles from the finished pastes (red markers).

The agglomeration of PB48 may have been a result of excessive sonication. Jiang and others [26] found that sonication of P25 dispersions for more than 30 seconds tended to increase agglomerate size. This is likely due to more frequent and increasingly forceful collisions occurring between dispersed nanoparticles resulting from sonication. The ball milled dispersion in this work was sonicated for 7 minutes in total, a procedure adapted from the mortar ground paste procedure. As the ball milled dispersion is already much better dispersed than the mortar ground dispersion prior to sonication, the sonication time for the ball milled dispersion can likely be shortened which could reduce agglomeration.

Approximately 10 μm-thick films of the mortar ground without roller mill treatment, mortar ground and passed 15 times through the roller mill, and 25 hour ball milled pastes were prepared by printing two layers of paste with the 110 TPI screen. After calcination, the films were dye loaded and assembled into sealed cells and had their J-V characteristics measured. The resulting performance data is shown in Table 3.2.

Several trends are evident in the performance data. On average, the thickness of films made from the two mortar ground pastes, PB42a and PB44, were similar to each other, though thicker than the ball milled paste PB46 by 1.6 μm. Despite the similar thicknesses, the PB42a film had much higher J_{sc} and η compared to the PB44 films. The J_{sc} and η values were much less consistent for the PB44 films as well. While having reduced performance compared to the PB42a films, the PB46 films also lacked extensive cracking and had more consistent performance than the PB44 films. Indeed, the performance of the PB46 films were on par with the much thicker PB44 films despite their reduced thickness.Examination of the optical and SEM images as well as the transmittance and reflectance spectra offer some potential explanations for the performance data.

Example optical images of the films are shown in Figure 3.5. The PB44 films showed a higher degree of cracking in the optical images than did the PB42a or PB44 films. The peeling associated with the cracking may reduce performance by hindering charge transfer from the TiO_2 film to the FTO substrate. The cracks and peeling could also increase recombination of electrons on the FTO with the I_3^- ions in the electrolyte. As the degree of cracking and peeling is not exactly consistent from one PB44 film to another, this could also account for the increased performance variability of the PB44 films.

The SEM images shown in Figure 3.6 seems to show better packing of the clusters in the PB46 film with fewer large voids compared to the PB42a and PB44 films. This improved packing likely results in higher internal surface area per unit volume of the

Paste	Processing			Film Area (cm^2)	Film Thickness (um)	V_{oc} (V)	J_{sc} (mA/cm^2)	FF	Efficiency (%)
	Mortar	Ball Mill	Passes Through Roller Mill						
PB42a	X		0x	0.232	11.1	0.731	10.90	0.681	5.43
				0.283	10.7	0.742	10.71	0.684	5.44
				0.246	9.9	0.746	9.79	0.702	5.13
				0.269	10.7	0.739	10.56	0.691	5.40
PB44	X		15x	0.272	11.6	0.731	7.83	0.697	3.99
				0.227	11.2	0.742	8.61	0.709	4.53
				0.271	9.5	0.742	9.93	0.701	5.17
PB46		X		0.249	9.1	0.735	8.85	0.701	4.56
				0.283	9.1	0.742	8.67	0.701	4.51
Average			PB42a	0.258	10.6	0.740	10.5	0.690	5.35
			PB44	0.257	10.8	0.739	8.8	0.702	4.56
			PB46	0.266	9.1	0.739	8.76	0.701	4.53
Sample Standard Deviation			PB42a	0.023	0.5	0.006	0.5	0.009	0.15
			PB44	0.026	1.1	0.007	1.1	0.006	0.6
			PB46	0.024	0.028	0.005	0.13	0.0003	0.04

Table 3.2: Performance data for films made from pastes of varying particle size distributions from different dispersion techniques.

TiO_2 film and should help increase dye loading.

The UV-Vis transmittance and diffuse reflectance spectra shown in Figure 3.7 suggest additional reasons for the differences in performance among the PB42a, PB44, and PB46 films. The DLS data for the three pastes shown in Figure 3.8 shows that the clusters in the PB42a paste were much better dissaggregated than in the PB44 paste. This likely explains the higher transmittance and lower diffuse reflectance of the PB42a film compared to the PB44 film. The higher transmittance and lower diffuse reflectance implies that less light is lost off the front of the PB 42a film and more light is penetrating the deeper regions of the film. To a certain extent, both of these factors should improve performance of a DSC as long as transmittance does not become so high that excessive light is lost out the back of the cell. The PB46

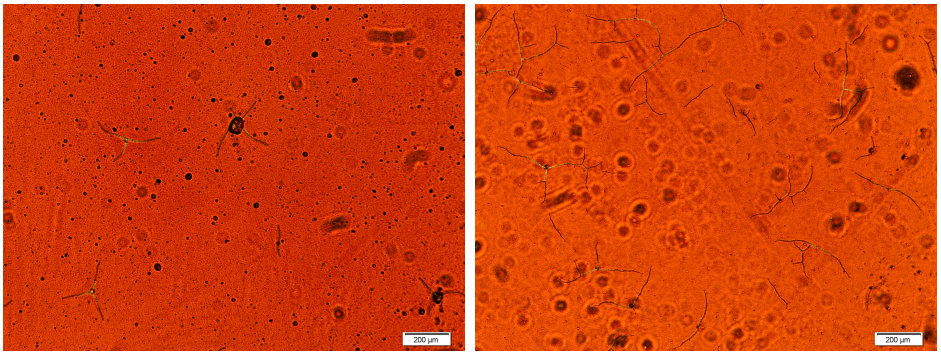

(a) PB42a.

(b) PB44.

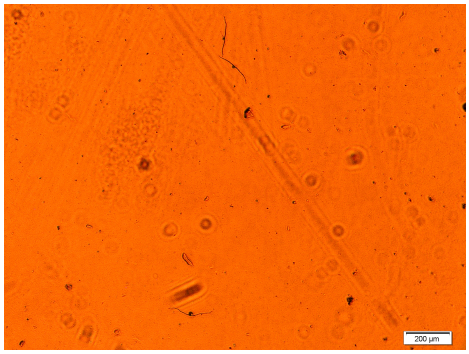

(c) PB46.

Figure 3.5: Optical microscope images of films made from mortar ground (PB42a), mortar ground and roller milled 15x (PB44), and ball milled pastes (PB46). Films have been dye loaded with N719.

film showed the highest transmittance and lowest diffuse reflectance of the three sets of films. This is consistent with the DLS data in Figure 3.8 and the SEM image in Figure 3.6c. The performance of the PB46 films is likely worse than the PB42a films despite the better optical characteristsics due to the lower thickness of the PB42a film.

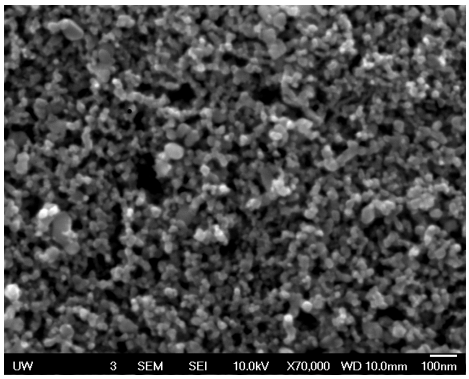

(a) PB42a.

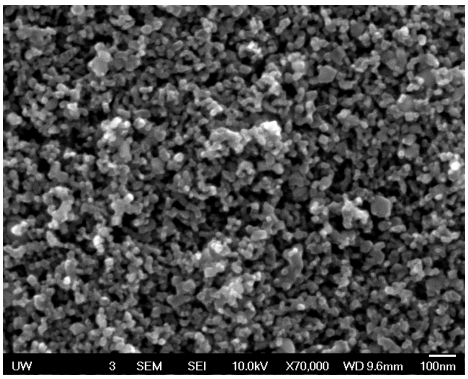

(b) PB44.

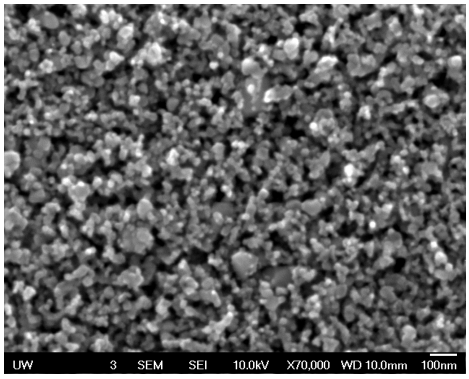

(c) PB46.

Figure 3.6: SEM images of films made from mortar ground (PB42a), mortar ground and roller milled 15x (PB44), and ball milled pastes (PB46).

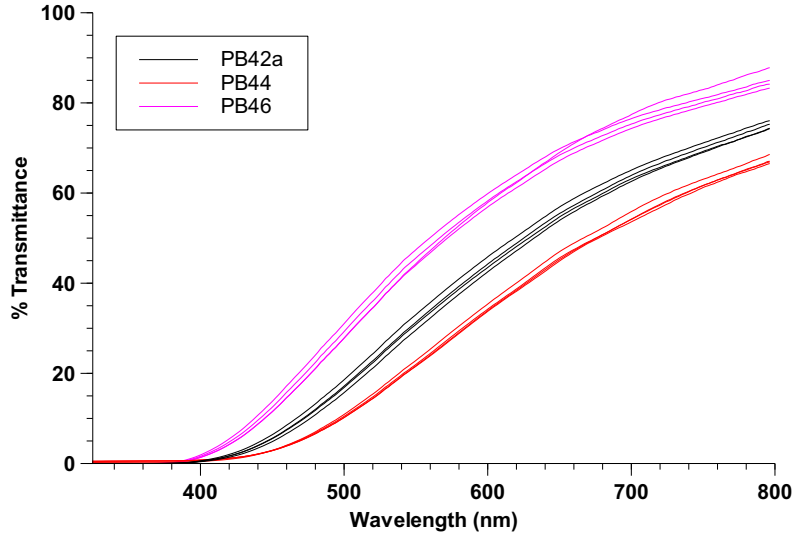

(a) Transmittance.

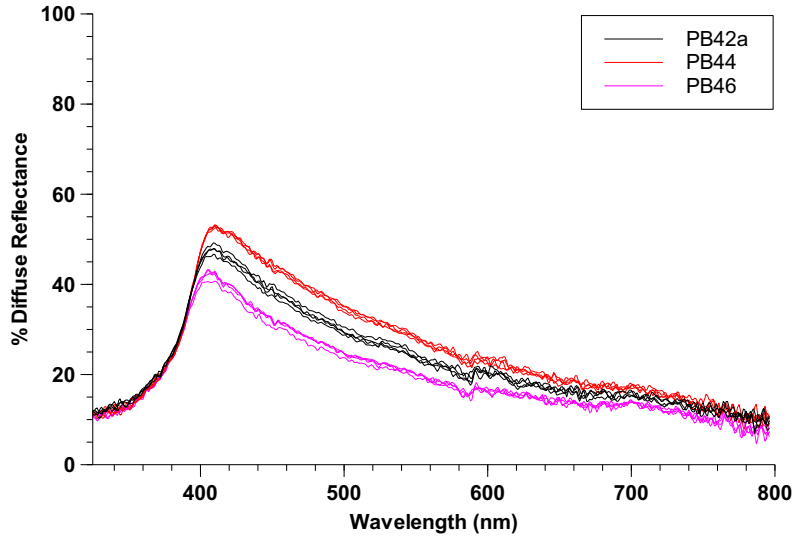

(b) Diffuse reflectance.

Figure 3.7: UV-Vis spectra of films made from mortar ground (PB42a), mortar ground and roller milled 15x (PB44), and ball milled pastes (PB46). Four films were tested for each paste. Films were not dye loaded and were tested wetted with acetonitrile and covered with a glass coverslip.

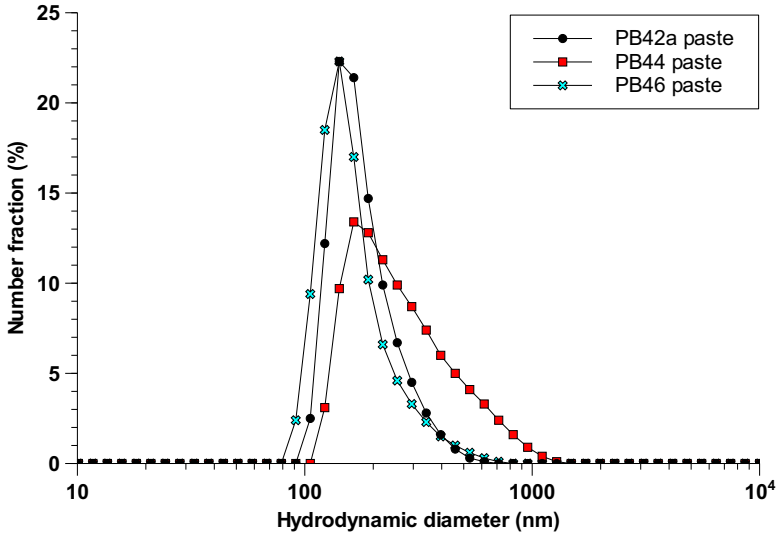

Figure 3.8: Particle size distributions for pastes PB42a (mortar ground, 0x roller mill), PB44 (mortar ground, 15x roller mill), and PB46 (ball milled) shown as number fraction. Particles were re-dispersed from pastes in ethanol.

3.1.2 Uniformity of Doctor Bladed Films

To evaluate the uniformity of films created by different doctor blade techniques, three different researchers created sets of TiO_2 films (films sets a, b, and c). Each researcher prepared their own TiO_2 paste using P25 nanoparticles. For film sets a and b, the P25 was ground in a mortar with a commercial binder. For film set c, the paste was prepared using the same ratios of P25, ethyl cellulose, and terpineol as in the mortar procedure in Figure 2.2. Mortar grinding was omitted, however, with all materials in the recipe being added to a single beaker and sonicated in a bath sonicator for the prescribed times in Figure 2.2. Note that the modified procedure for set c films resulted in poorly disaggregated nanoparticles compared to those in the pastes prepared with the mortar grinding and probe sonicator. For film sets a and b, an approximately 5 mm by 5 mm area was masked off on the substrate using a single

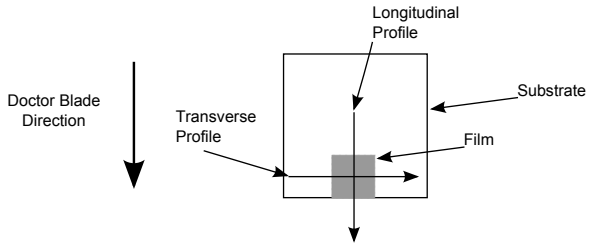

Figure 3.9: Profile directions for contact profilometer measurements of film thickness relative to doctor blade direction.

layer of Scotch® tape. For film set c, a larger area was doctor bladed and the excess film scraped away.

For each film set, a longitudinal and transverse film thickness profile was collected using a Tencor Instruments P15 contact profilometer. The directions of the profiles relative to the doctor blade direction are shown in Figure 3.9. The resulting profiles are shown in Figure 3.10. Both film sets with untrimmed edges (sets a and b) show significant thickening near the edges of the film. Significant thickening at the edges is not observed in film set c except for sample c2 on the longitudinal profile. The thickening of c2 on the longitudinal profile, however, resulted from poor technique in scraping away the excess film and can be avoided by using greater care to push the microscope slide used to scrape the excess film away from the main area of the film when applying the slide to the film surface. If the slide is applied vertically or slightly back towards the main area of the film, then a small amount of film will be peeled up from the substrate resulting in a bump at the edge of the film.

The profiles of film set c also show greater uniformity in average thickness across the profile of a single sample. Film sets a and b show significant variation in average thickness across the profiles. This is variation in thickness is likely due to the difficulty in pulling the doctor blade with uniform speed over the substrate. The variation in doctor blade speed for film sets a and b may have resulted from pulling the doctor

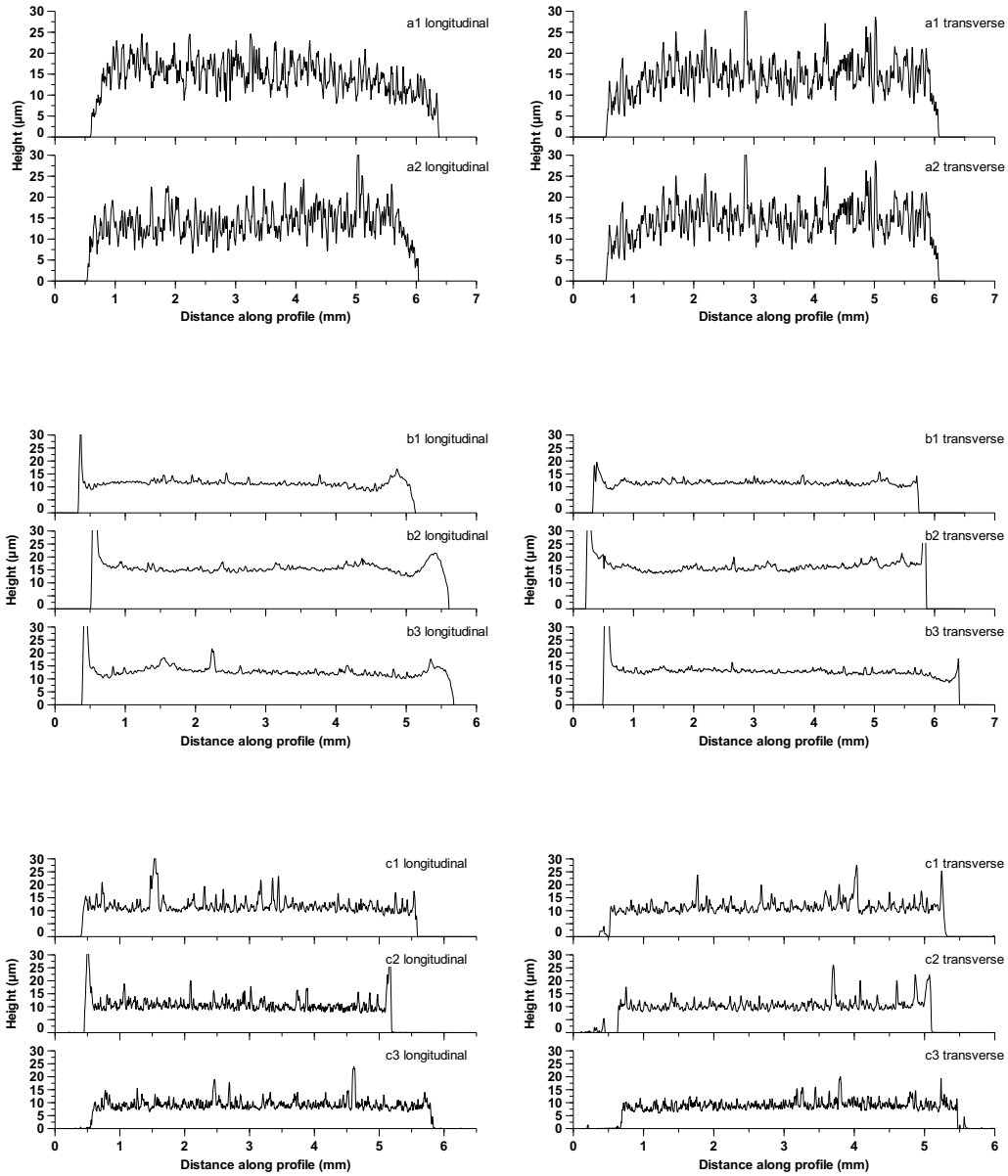

Figure 3.10: Thickness profiles of doctor bladed film sets a , b, and c.

blade across the transition from two layers to one layer of tape as is necessary with the masking technique used in film sets a and b. In film set c, the doctor blade always

rested on a single layer of tape.

3.1.3 Comparison of Films Created Using Doctor Blade and Screen Printing Techniques

To compare the performance of TiO_2 films created using the doctor blade and screen printing techniques, eight films were created using the P25 paste PB42a. Samples b77s01 through b77s04 were screen printed two layers thick using the 110 TPI screen, and samples b77s05 through b77s08 were doctor bladed using a single layer of Scotch® tape as a spacer. The edges of both sets of films were scraped away using a microscope slide to achieve a film area of ~25 mm^2. After calcination of the films, longitudinal and transverse film thickness profiles were measured using the P15 contact profilometer with profiles oriented as shown in Figure 3.9. The resulting longitudinal and transverse profiles are shown in Figures 3.11 and 3.12 respectively. The profiles show that the doctor blade and screen printing techniques can yield films of uniform thickness if the edges are trimmed away. The doctor bladed films are slightly thicker than the screen printed film, with average thicknesses of 10.5 μm and 9.0 μm respectively.

The b77 films were assembled into sealed DSCs using the Dyesol HPE1 electrolyte and tested for performance. The DSC performance is given in Table 3.3. The screen printed and doctor bladed films on average did not show any significant difference in performance.

3.2 Influences of Device Structure and Assembly

3.2.1 Vacuum Dye Loading

For sufficient loading of the TiO_2 film, the dye must penetrate as many of the pores in the film as possible. Penetration of the dye is accomplished by capillary forces. There is the possibility that air trapped in the pores of the film may prevent dye penetration and thus reduce dye loading. To evaluate whether trapped air could

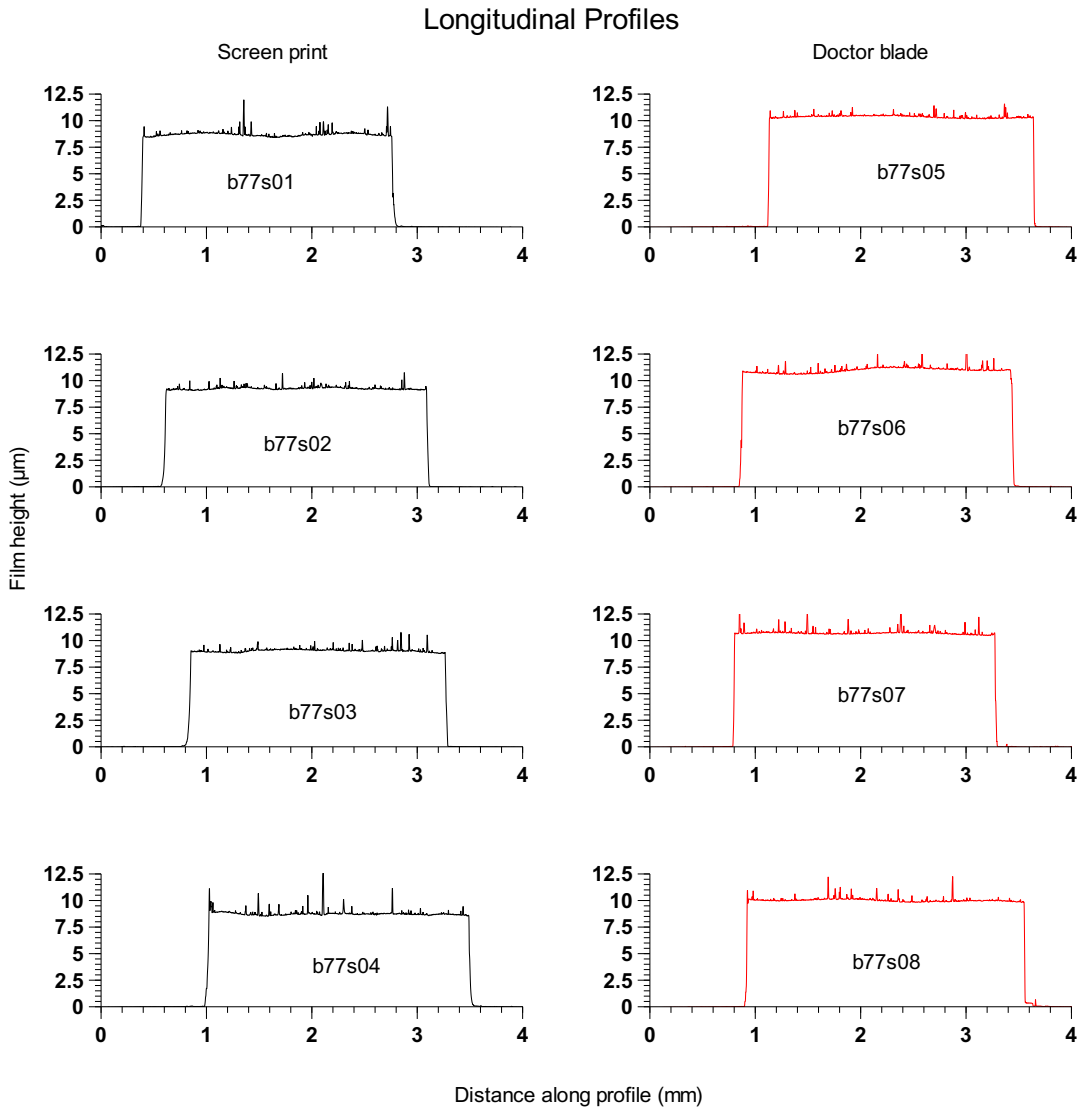

Figure 3.11: Longitudinal film thickness profiles of screen printed and doctor bladed films.

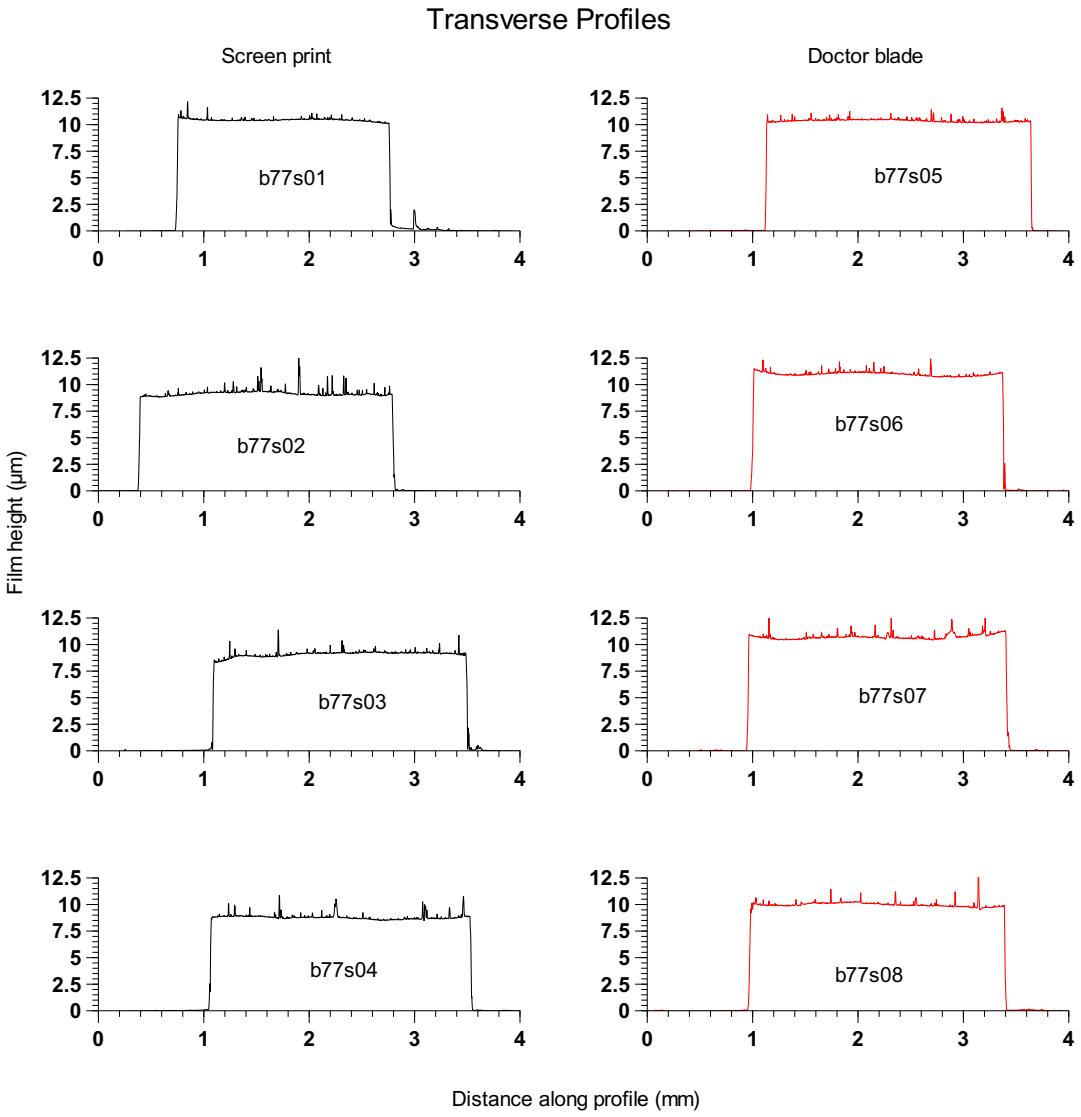

Figure 3.12: Transverse film thickness profiles of screen printed and doctor bladed films.

Technique	Sample	Film Area (cm^2)	V_{oc} (V)	J_{sc} (mA/cm^2)	FF	Efficiency (%)	Average			
							V_{oc} (V)	J_{sc} (mA/cm^2)	FF	Efficiency (%)
Screen Print	b77s01	0.234	0.739	8.94	0.689	4.55	0.75	8.6	0.701	4.49
	b77s02	0.240	0.769	8.22	0.711	4.49				
	b77s03	0.234	0.746	8.71	0.701	4.56				
	b77s04	0.246	0.742	8.40	0.702	4.38				
Doctor Blade	b77s05	0.205	0.746	9.18	0.707	4.84	0.741	9.17	0.692	4.70
	b77s06	0.246	0.739	9.42	0.673	4.68				
	b77s08	0.257	0.739	8.90	0.696	4.57				

Table 3.3: Comparison of the performance of screen printed and doctor bladed films.

affect dye loading and negatively impact DSC performance, TiO_2 films were placed into a glass container, immersed in dye, and then the container was placed in a vacuum chamber which was evacuated to 100 mbar for 5 minutes. After exposure to vacuum, air was reintroduced to the chamber and additional TiO_2 films were added to the dye solution. After 24 hours of dye loading, the cells were removed from the dye solution, rinsed with ethanol, dried, and tested in the open configuration. As shown in Table 3.4, the vacuum dye loading did not improve the performance of the DSCs.

Vacuum	Voc (V)	Jsc (mA/cm^2)	FF	Efficiency (%)	Average			
					Voc (V)	Jsc (mA/cm^2)	FF	Efficiency (%)
Yes	0.739	12.5	0.496	4.58	0.749	11.5	0.518	4.45
	0.746	10.7	0.530	4.23				
	0.761	11.3	0.529	4.54				
No	0.743	12.9	0.540	5.15	0.744	11.6	0.540	4.68
	0.746	10.4	0.541	4.21				

Table 3.4: Performance of DSCs that underwent vacuum dye loading and dye loading at atmospheric pressure.

Sealing	Sample	Film thickness (um)	Film Area (cm^2)	V_{oc} (V)	J_{sc} (mA/cm^2)	FF	Efficiency (%)
Unsealed	B53S5a	16.7	0.266	0.671	10.9	0.604	4.43
	B53S11a	13.6	0.300	0.697	9.87	0.626	4.31
Epoxy	B53S6b	16.8	0.308	0.645	10.5	0.629	4.25
	B53S12a	15.5	0.357	0.660	9.64	0.628	3.99
Heat	b53s8a	16.6	0.310	0.656	11.3	0.614	4.55
	b53s9c	14.7	0.291	0.641	10.7	0.625	4.29

Table 3.5: Performance of unsealed, heat sealed, and epoxy sealed DSCs.

3.2.2 Sealing

DSCs may be tested in a sealed or unsealed configuration as discussed above. To determine whether sealing affects DSC performance, three sets of films were screen printed from the same P25 TiO_2 paste. Two sets of cells were tested sealed, and one set was tested unsealed. Of the two sets of sealed cells, one set was sealed using thermoplastic film, the other set was sealed with epoxy. The results of the J-V tests are given in Table 3.5. The three sets of cells do not show a significant difference in performance for the initial test.

As shown in Figure 3.13, repeated testing of the same cell over a period of approximately two minutes shows that the unsealed cell rapidly decreases in performance, while the sealed cells are more stable. The decrease in performance of the unsealed cells is likely due to rapid loss of solvent from the electrolyte during testing. For short term tests, unsealed cells give acceptable performance. For longer term testing such as that required for EIS, cyclic voltametry, or incident photon conversion efficiency testing, sealed DSCs should be used to prevent solvent loss.

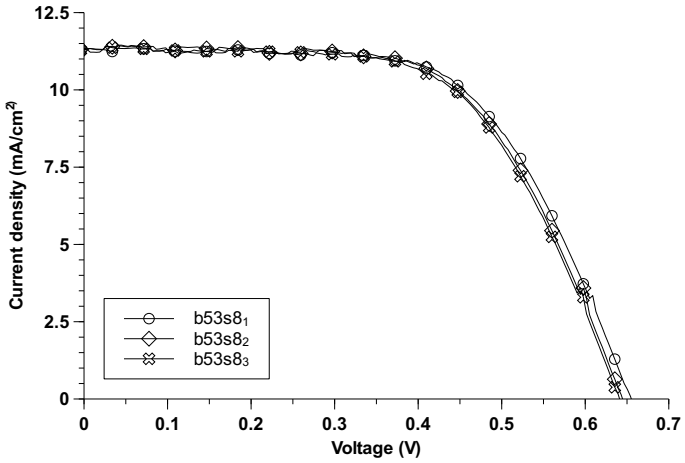

(a) Heat sealed.

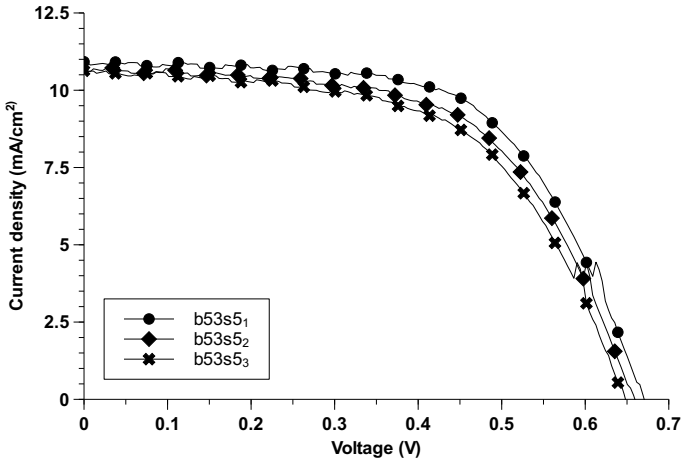

(b) Unsealed.

Figure 3.13: Stability of performance for heat sealed and unsealed DSCs. DSCs were repeatedly tested over a period of approximately 2 minutes.

3.2.3 Electrolytes

Previous research has shown that the electrolyte used in DSC fabrication has a significant impact on DSC performance [17, 9, 31]. To compare the performance of

Electrolyte	Sample	Film Area (cm^2)	Voc (V)	Jsc (mA/cm^2)	FF	Efficiency (%)
Dyesol HPE1	b54s2c	0.305	0.64	10.88	0.64	4.43
	b54s4c	0.294	0.63	10.70	0.66	4.42
	b54s5c	0.259	0.61	10.09	0.68	4.22
	b54s8c	0.261	0.64	9.91	0.66	4.16
Lab	b54s1c	0.271	0.62	13.41	0.58	4.82
	b54s3c	0.267	0.61	12.95	0.58	4.60
	b54s6c	0.296	0.58	12.53	0.61	4.47
	b54s7c	0.260	0.61	13.13	0.60	4.87

Average	Dyesol HPE1	0.28	0.63	10.4	0.66	4.3
	Lab	0.27	0.61	13.0	0.59	4.7
Sample Standard Deviation	Dyesol HPE1	0.08	0.020	0.5	0.018	0.14
	Lab	0.016	0.015	0.4	0.014	0.18

Table 3.6: Performance data for initial comparison of lab and Dyesol HPE1 electrolytes.

DSCs using the lab electrolyte versus the Dyesol HPE (Dyesol HPE1), cells with approximately 10 μm-thick P25 TiO_2 films were sealed and vacuum infiltrated with electrolyte as described previously. The cells were then tested for their J-V performance. As shown in Figure 3.14 and Table 3.6, DSCs using the lab electrolyte had higher J_{sc}'s, while the V_{oc}'s were approximately the same.

The initial comparison of the lab electrolyte and Dyesol HPE used a batch of Dyesol HPE that had been opened approximately 8 months prior to the test. Due to concerns about contamination of the Dyesol HPE1 with water absorbed from the atmosphere, a fresh batch of Dyesol HPE (Dyesol HPE2) was ordered and the test was repeated. Due to problems with press used to seal the cells, the TiO_2 films used in the repeat test were not immediately sealed and infiltrated with electrolyte after dye loading. Instead, the films were stored under vacuum and protected from light

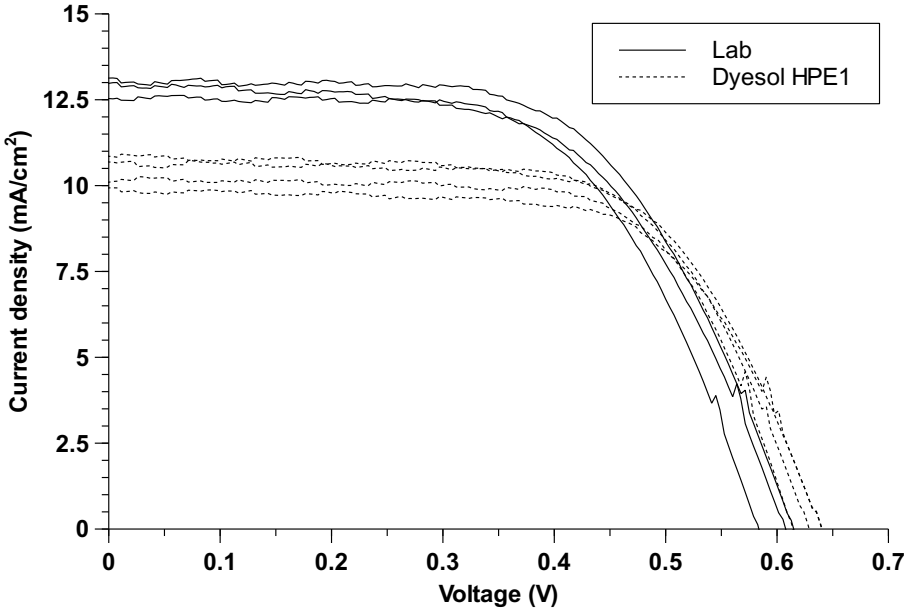

Figure 3.14: J-V plot for initial comparison of lab and Dyesol HPE1 electrolytes.

for 15 days until the press was repaired. While this led to a significant decrease in performance as shown in Table 3.7 when compared to the results in Table 3.6, the performance trends were the similar, though less pronounced. The DSCs using the lab electrolyte still had higher J_{sc}'s than either of the Dyesol HPEs. Interestingly, the two Dyesol electrolytes performed about the same, suggesting that the electrolytes, when stored away from light and in sealed containers, maintain their performance for many months. Given the small number of samples and the variability their performance, however, the results may not be statistically significant.

To evaluate the reason for the improved performance of the lab electrolyte over the Dyesol HPE, three DSCs using the three different electrolytes were tested using EIS. EIS measurements were carried out under dark conditions and at a voltage bias of -0.75 V. The Nyquist plots for the DSCs is shown in Figure 3.15. Typically, the Nyquist plot for a DSC exhibits three semi-circles: one at high frequencies ($\sim 10^5$-10^3

Electrolyte	Sample	Film Area (cm^2)	Voc (V)	Jsc (mA/cm^2)	FF	Efficiency (%)
Lab	b65s3a	0.300	0.637	5.59	0.687	2.45
	b65s4a	0.298	0.634	5.77	0.685	2.50
	b65s9a	0.283	0.618	4.57	0.686	1.94
Dyesol HPE1	b65s7b	0.311	0.615	5.80	0.680	2.42
	b65s8c	0.296	0.630	4.79	0.702	2.12
	b65s11a	0.289	0.634	4.21	0.703	1.88
Dyesol HPE2	b65s5a	0.278	0.622	4.91	0.698	2.13
	b65s6a	0.300	0.633	5.12	0.696	2.26
	b65s12a	0.289	0.618	3.93	0.723	1.76
Average	Lab	0.294	0.630	5.31	0.686	2.30
	Dyesol HPE1	0.299	0.626	4.93	0.695	2.14
	Dyesol HPE2	0.289	0.625	4.65	0.706	2.05
Sample Standard Deviation	Lab	0.009	0.010	0.6	0.0011	0.3
	Dyesol HPE1	0.011	0.010	0.8	0.0129	0.27
	Dyesol HPE2	0.011	0.008	0.6	0.014832	0.26

Table 3.7: Performance data for second comparison of lab, Dyesol HPE1, and HPE2 electrolytes.

Hz) associated with the charge transfer at the electrolyte-Pt film interface, one at medium frequencies ($\sim 10^3$-10^1 Hz) associated with charge transfer at the electrolyte-TiO_2 film interface, and one at low frequencies ($\sim 10^1$-10^{-1} Hz) associated with the charge transport within the electrolyte [46]. The Nyquist plots in Figure 3.15 only shows well developed semicircles for the high and medium frequency ranges, with the low frequency semicircle indistinct from the medium frequency semicircle. Note that on the Nyquist plots, the frequency of the applied voltage oscillation decreases from left to right.

Charge transport and transfer resistances are obtained by fitting an equivalent circuit to the impedance data. In the equivalent circuit used to fit the Nyquist plot for the TiO_2-Pt cells, the charge transfer resistance at the electrolyte-TiO_2 film interface and at the electrolyte-Pt film interface are modeled using resistive elements ($R_{ct\text{-}TiO_2}$

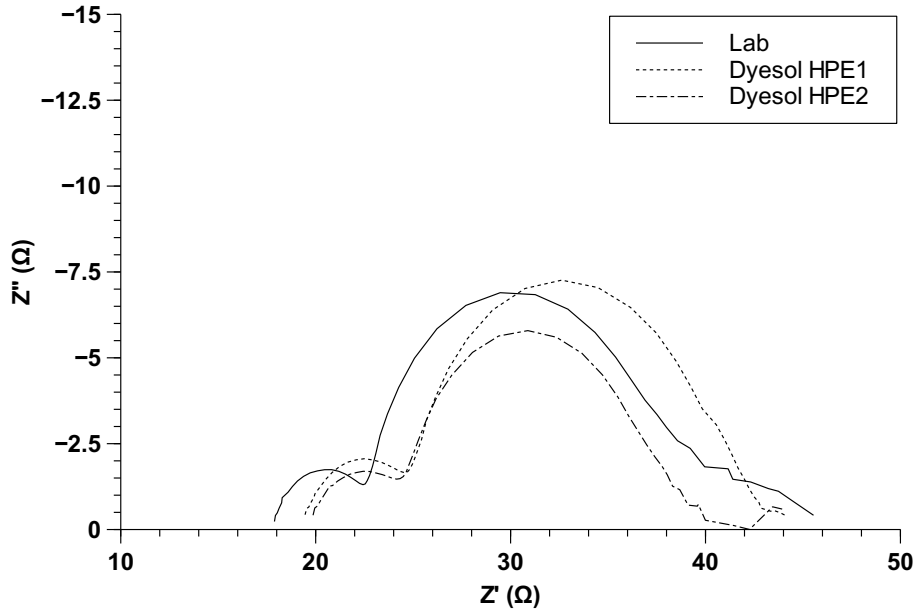

Figure 3.15: Nyquist plot for TiO_2-Pt cells. The larger semicircle relates to charge transfer at the electrolyte-TiO_2 film interface, while the smaller semicircle relates to charge transfer at the electrolyte-Pt interface. The semicircle due to the I_3^- diffusion impedance (far right) is poorly developed.

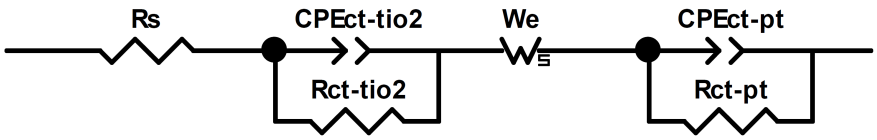

Figure 3.16: Equivalent circuit used to fit impedance data for the TiO_2-Pt cells.

and $R_{ct\text{-}Pt}$), and constant phase elements ($CPE_{ct\text{-}TiO_2}$ and $CPE_{ct\text{-}Pt}$) are used to model the double-layer capacitance as shown in Figure 3.16. The CPEs are used instead of capacitances due to the porous nature of the TiO_2 and Pt films on the anode and cathode respectively [17]. The impedance due to I_3^- diffusion within the electrolyte was modeled using a finite length Warburg element (We).

The equivalent circuit was fitted to the data range over which the impedances due to the two electrolyte-film interfaces and diffusion of I_3^- ions within the electrolyte dominated the response of the DSC. The equivalent circuit in Figure 3.16 fit the data quite well, and an example fit is shown in Figure 3.17.

As mentioned above, the semicircle on the Nyquist plots due to the I_3^- diffusion impedance for the TiO_2-Pt cells was poorly developed and indistinct from the semicircle associated with the electrolyte-TiO_2 interface. To better evaluate the diffusion impedance as well as repeat the measurement of $R_{ct\text{-}Pt}$ under different conditions, the EIS spectrum of a sealed cell consiting of dual Pt electrodes was taken following the procedure of Hauch and Georg [17]. The area of the platinum film exposed to electrolyte was 0.8 cm^2. The Pt-Pt cells were tested under dark conditions at a bias voltage of 0 V. The Nyquist plots for the Pt-Pt cells are shown in Figure 3.18. In contrast to cells that have a TiO_2 electrode and Pt electrode, the Nyquist plot shows well developed semicircles related to the electrolyte-Pt interface (larger) and the I_3^- diffusion impedance (smaller).

The equivalent circuit used to fit the Pt-Pt cell impendance data is shown in

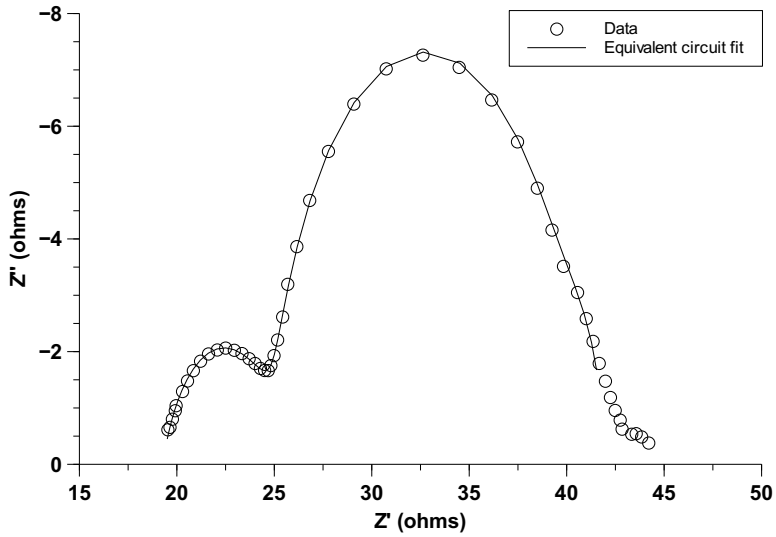

Figure 3.17: Example of equivalent circuit fit to impedance data for the circuit shown in Figure 3.16. The equivalent circuit used for the fit is unable to fit the data points at the lowest frequencies, so those date points were not included in the fit.

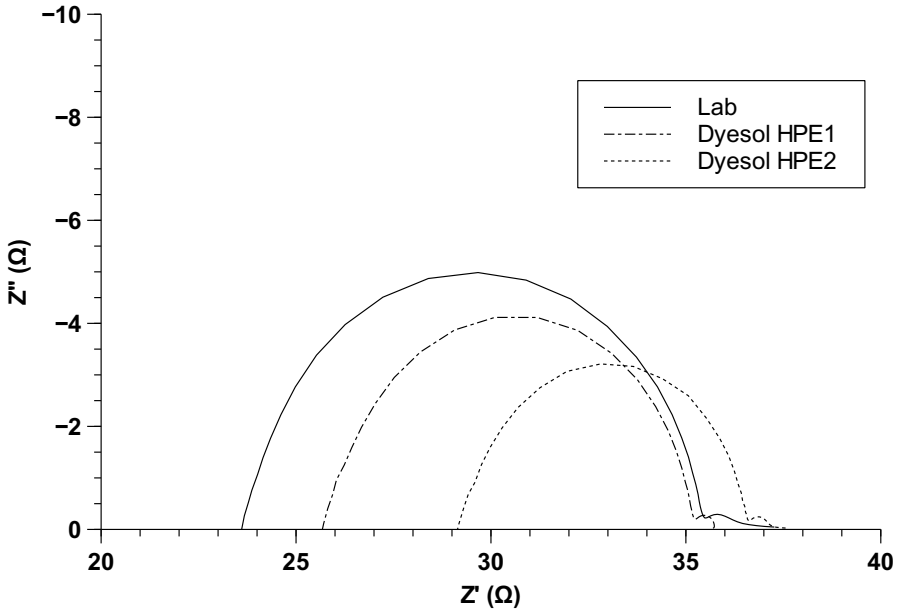

Figure 3.18: Nyquist plot for Pt-Pt cells. The larger semicircle relates to charge transfer at the electrolyte-Pt interface, while the small semicircle is a result of the I_3^- diffusion impedance.

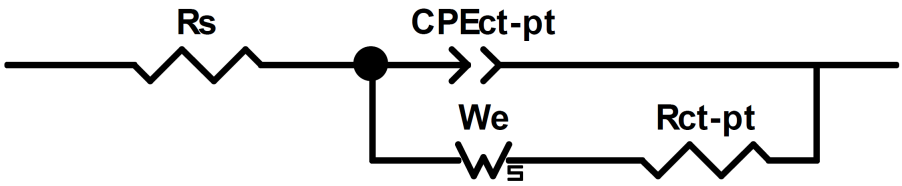

Figure 3.19: Equivalent circuit fit to impedance data for the Pt-Pt cells.

Figure 3.19.

The finite length Warburg impedance is determined by the following equation:

$$Z_W = R_N \frac{1}{\sqrt{\frac{i\omega}{K_N}}} \tanh \sqrt{\frac{i\omega}{K_N}} \tag{3.1}$$

where $K_N = D/\delta^2$. D is the diffusion coefficient of triiodide in the electrolyte and δ is the thickness of the diffusion layer, taken as $\delta = \frac{l}{2}$ where l is the distance between the electrodes and is taken to be the 30 μm thickness of the thermoplastic film. Fitting the equivalent circuit to the impedance data yields a value for K_N which can then be used to calculate D.

The results of the $R_{ct\text{-}Pt}$, $R_{ct\text{-}TiO_2}$, and $D_{I_3^-}$ are given in Table 3.8, and are inconsistent. The $R_{ct\text{-}TiO_2}$ value from the TiO_2 film-Pt cell is higher for the lab electrolyte than for the Dyesol HPE2, suggesting that the higher J_{sc} associated with the lab electrolyte could result from reduced recombination with the I_3^- ions in the electrolyte. The $R_{ct\text{-}TiO_2}$ value for the Dyesol HPE1 electrolyte, however, is a little higher than that for the lab electrolyte, suggesting that another factor may play a role in the better performance of the lab electrolyte. The $R_{ct\text{-}Pt}$ value for the lab electrolyte is somewhat smaller than that for either Dyesol electrolyte, so perhaps faster reduction of the I_3^- at the cathode explains the better performance of the lab electrolyte. The results from the Pt-Pt cells, however, show the opposite trend in $R_{ct\text{-}Pt}$, with lower

values for the Dyesol electrolytes and a higher value for the lab electrolyte. Furthermore, the $D_{I_3^-}$ values imply that the I_3^- ions in the Dyesol electrolytes should diffuse more quickly than in the lab electrolyte, so the I_3^- diffusion rate does not explain the better performance.

As only one sample for each electrolyte was tested in the TiO_2 film-Pt and Pt-Pt cell configurations, variability in the surface area of the TiO_2 and Pt films could account for the inconsistent EIS results. This experimental difficiency could be addressed by repeating the experiment with more cells to constrain the variability in the EIS results. The challenge would be in getting enough films with the same area and thickness to enable valid comparisons. Agreement between the I_3^- diffusion coefficients calculated from the TiO_2-Pt and Pt-Pt cells suggests that the diffusion coefficient is well determined. Furthermore, the measured values are similar to those reported for other triiodide-acetonitrile based electrolytes [17].

Electrolyte	Electrode Setup				
	TiO_2-Pt			Pt-Pt	
	$R_{ct\text{-}TiO2}$ (Ω)	$R_{ct\text{-}Pt}$ (Ω)	$D_{I_3^-}$ (cm^2/s)	$R_{ct\text{-}Pt}$ (Ω)	$D_{I_3^-}$ (cm^2/s)
Lab	15.0	4.9	1.14E-05	5.8	1.16E-05
Dyesol HPE1	15.7	5.6	1.27E-05	4.6	1.49E-05
Dyesol HPE2	12.5	5.1	1.76E-05	3.6	1.86E-05

Table 3.8: Results of EIS testing of the three electrolytes.

3.3 Conclusions

The two principal goals of this research were to evaluate the relative merits of different paste preparation and DSC assembly technqiues and to find a suite of methods that reliably produced DSCs based on the P25 nanoparticle with efficiencies of ∼6%. While the efficiency goal was not achieved, important information on the paste preparation

and assembly techniques was gathered that will enable reliable fabrication of DSCs and suggest directions for further research that may lead to the achievement of the efficiency goal.

3.3.1 Preparation of the Photoanode Film

TiO_2 Paste

The most important experimental results of this work concern the effect of paste making procedure on the distribution of cluster sizes in the paste and the resulting effect on the mechanical and optical properties of the films. DLS measurements of mortar ground pastes with varying degrees of roller milling show that the final cluster size distribution of the paste is determined by the mortar grinding step. Roller milling has minimal impact on the cluster size distribution. This result is likely due to the spacing between the rollers of the roller mill. On the Exakt50 roller mill, the narrowest spacing is on the order of several microns, and the spacing can increase during roller milling as a result of pressure in the paste between the rollers forcing the rollers apart. When the aggregate size is significantly less than the roller spacing, the shearing forces between the rollers are not high enough to tear the aggregates apart. Demonstration of the negligible impact of roller milling on particle size distribution in DSC pastes has not been reported elsewhere in the literature, despite other researchers using the paste making method that includes roller milling as the last step [22, 50]. The implication that roller milling can be omitted in paste preparation significantly simplifies paste preparation and obviates the need for labs to purchase an expensive roller mill to make TiO_2 pastes for DSCs.

The DLS results also show that the particle size distribution achievable with mortar grinding is difficult to control. A smaller cluster size distribution can be achieved with ball milling, and using DLS to monitor the particle size distribution during ball milling should allow for repeatable results. As the mortar grinding process proceeds

much more quickly than ball milling, DLS verification of mortar ground paste cluster size distribution is more difficult to carry out without impacting the results of the mortar grinding. Given the small cluster size and repeatability of the ball milling technique, further research efforts towards a high performance P25 paste should use that disaggregation method.

Achieving a small cluster size distribution is important to DSC performance for several reasons. Large clusters act as nucleation points for cracks in the film, and cracks have a negative impact on DSC performance by causing peeling of the film off the substrate. Large clusters may also cause cracking and peeling by decreasing film intercluster bond strength and substrate adhesion strength by reducing packing density as well as contact area both between clusters and between clusters and the substrate. A similar decrease in film cracking with decreasing cluster size was observed by Ito and others [25] when comparing pastes in which the TiO_2 nanoparticles were dispersed by mortar grinding with pastes in which the particles were dispersed by mortar grinding and chemical treatment.

Additional studies to verify the effect of cluster size on film intercluster bond and adhesion strength would be useful. Intercluster bond strength could be measured using Vickers indent testing with acoustic emission monitoring [52]. The film adhesion strength could be measured through a laser spallation technique [45]. Ito and others [22] have suggested that a pretreatment of the FTO substrate with titanium tetrachloride can improve film adhesion to the substrate. Verifying this assertion would be helpful to determining whether this added processing step is important to DSC fabrication.

Decreasing cluster size also reduces excessive diffuse reflectance off the surface of the film as observed in the diffuse reflectance spectra. Decreased diffuse reflectance should improve DSC performance by allowing light incident on the DSC to penetrate further into the cell. The improved performance associated with decreased cluster size has been noted by other workers who found improved light absorption [25] and

film transparency [50].

Improved nanoparticle dispersion also improves DSC performance by increasing film internal surface area and, in turn, dye loading. Ito et al. [25] found an increase in dye loading associated with the ball milled/chemically dispersed pastes as compared to mortar ground paste when dye loading was measured using dye desorption experiments. EIS measurements also suggested that the ball milled/chemically dispersed pastes had higher internal surface areas compared to the films based on mortar ground pastes [25].

Screen Printing and Doctor Blade Techniques

While both the doctor blade and screen printing techniques have been used to make TiO_2based DSCs, a side-by-side comparison of the films produced by the two techniques has not been found in the literature. Evaluation of the two methods show that both can produce films of comparable thickness and uniformity from the same TiO_2 paste if the edges of the films are scraped away after calcination. DSCs created using films from each method do not show significant differences in either the average or repeatability of DSC performance. This result is consistent with the data shown in Table 1.1 where both doctor bladed and screen printed P25 films produced DSCs with efficiencies around 6%. Thus the choice between methods comes to one of convenience and control over the photoanode film thickness. If the screen printing were carried out by machine rather than by hand as was done in this work, the variability in the performance of DSCs printed at the same time might be reduced relative to the doctor bladed films. A comparison amongst hand doctor bladed, hand screen printed, and machine screen printed photoanode films would address this question.

3.3.2 Device Assembly

Dye Loading and Device Sealing

The standard dye loading procedure used in the literature is to simply immerse the photoanode film into the dye solution for approximately 24 hours. It would seem, however, that it would be difficult to remove all of the air from the pores in the TiO_2 film merely by immersing the film in the dye solution. Furthermore, a review of the literature did not find any discussion of exposing the dye solution to vacuum when dye loading the TiO_2 film. Comparison of the standard method with a vacuum dye loading procedure in which the dye solution with the immersed photoanode films is exposed to a vacuum of 100 mbar for five minutes prior to dye loading for 24 hours at atmospheric pressure showed no significant difference in DSC performance. This suggests that air trapped in the pore space between TiO_2 nanoparticles does not significantly inhibit dye penetration into the pores. Given this result, it is likely that capillary forces in the film are high enough to pull the dye solution into most of the film. If there are pores that remain filled with air, the pressures generated in the pore space may be high enough to cause the air to dissolve in the dye solution.

A rough calculation suggests why exposing the film to vacuum makes little difference in dye loading. Capillary pressure ΔP in a tube of radius R can be calculated using the Young-Laplace equation:

$$\Delta P = \frac{2\gamma \cos\theta}{R} \tag{3.2}$$

where γ is the surface tension and θ is the contact angle. For an air-ethanol interface, the surface tension is 0.0223 N/m [2]. While a value for the contact angle for ethanol on a TiO_2 surface could not be found in the literature, the contact angle for water on TiO_2 in air is about 72° [35]. The contact angle for ethanol on TiO_2 in air is likely to be less than that of water, so we take $\theta = 72°$ as an upper limit. Assuming a pore radius of 25 nm, which seems reasonable given the SEM images

above, ΔP is 0.55 MPa. Assuming that dye solution in the pores is at atmospheric pressure of about 0.1 MPa, the fractional decrease in pressure in exposing the dye to vacuum is only 15%. If the contact angle is only 36°, then ΔP is 1.4 MPa and the fractional decrease in pressure achieved using vacuum is only 7%. Such small fractional decreases in pressure are unlikely to cause large volumes of air to escape from the pores of the film.

All of the P25-based DSCs reviewed for this work either used sealed configuations for testing, or did not specify how or if the cells were sealed during testing, so comparing the performance of unsealed and sealed cells directly is quite useful. The comparison of unsealed, epoxy sealed, and thermoplastic gasket sealed DSC performance did not show a consistent difference in performance. This result is somewhat surprising as the unsealed and epoxy sealed cells have larger areas of FTO substrate exposed to the electrolyte than the gasket sealed cells. The FTO substrate-electrolyte interface is thought to be one of the locations where the recombination reaction between electrons and I_3^- in the electrolyte occurs leading to performance losses in the DSC [24] , so increasing the area of this interface in the unsealed and epoxy sealed DSCs should cause reduced performance compared to the gasket sealed cells. This apparent contradiction could be a statistical result of the low numbers of DSCs tested in the different sealing configurations, and this comparison should be repeated with larger numbers of cells.

Electrolyte Performance

The improved performance of the lab electrolyte compared to the Dyesol HPE is also quite significant. EIS results suggest that the improved performance is coming from decreased recombination rate at the electrolyte-TiO_2 film interface and/or faster reduction of I_3^- at the electrolyte-Pt interface, though the results for the latter are not consistent between TiO_2-Pt and Pt-Pt cell configurations. The decreased diffusion coefficient for the lab electrolyte compared to the Dyesol HPE indicates that the I_3^-

diffusion rate is not responsible for the improved performance of the lab electrolyte.

Additional work to determine the reason for the improved performance of the lab electrolyte should be carried out. This work would necessarily start with the determining the detailed composition of the Dyesol HPE and comparing it to that of the lab electrolyte. One potential candidate for the reduced recombination at the electrolyte-TiO_2 interface is guanidinium thiocyanate, which has been found to reduce recombination [12]. Measurement of the area of the Pt-electrolyte interface would enable calculation of the charge transfer resistance per unit area at the interface and could resolve the disagreement in measurement of that charge transfer resistance between the TiO_2-Pt and Pt-Pt cell configurations.

REFERENCES

[1] M. Adachi, M. Sakamoto, J. Jiu, Y. Ogata, and S. Isoda. Determination of parameters of electron transport in dye-sensitized solar cells using electrochemical impedance spectroscopy. *The Journal of Physical Chemistry B*, 110(28):13872–13880, 2006.

[2] A. W. Adamson and A. P. Gast. *Physical chemistry of surfaces*. Wiley, New York, 1997.

[3] T. R. Andersen, T. T. Larsen-Olsen, B. Andreasen, A. P. L. Böttiger, J. E. Carlé, M. Helgesen, E. Bundgaard, K. Norrman, J. W. Andreasen, M. Jørgensen, and F. C. Krebs. Aqueous processing of low-band-gap polymer solar cells using roll-to-roll methods. *ACS Nano*, 5(5):4188–4196, 2011.

[4] D. Arvizu, P. Balaya, L. F. Cabeza, K. G. T. Hollands, A. Jäger-Waldau, M. Kondo, C. Konseibo, V. Meleshko, W. Stein, Y. Tamaura, H. Xu, and R. Zilles. Direct solar energy. In *IPCC Special Report on Renewable Energy Sources and Climate Change Mitigation*, pages 333–400. Cambridge University Press, Cambridge, United Kingdom and New York, NY, USA, 2011.

[5] S. Beucher and C. Lantujoul. Use of watersheds in contour detection. In *Proceedings of the International Workshop on Image Processing, Real-time Edge and Motion Detection/Estimation*, 1979.

[6] D. M. Chapin, C. S. Fuller, and G. L. Pearson. A new silicon p-n junction photocell for converting solar radiation into electrical power. *Journal of Applied Physics*, 25(5):676–677, 1954.

[7] T. P. Chou, Q. Zhang, and G. Cao. Effects of dye loading conditions on the energy conversion efficiency of ZnO and TiO_2 dye-sensitized solar cells. *The Journal of Physical Chemistry C*, 111(50):18804–18811, 2007.

[8] L. Dou, J. You, J. Yang, C.-C. Chen, Y. He, S. Murase, T. Moriarty, K. Emery, G. Li, and Y. Yang. Tandem polymer solar cells featuring a spectrally matched low-bandgap polymer. *Nat Photon*, 6(3):180–185, Mar. 2012.

[9] F. Fabregat-Santiago, J. Bisquert, G. Garcia-Belmonte, G. Boschloo, and A. Hagfeldt. Influence of electrolyte in transport and recombination in dye-sensitized solar cells studied by impedance spectroscopy. *Solar Energy Materials and Solar Cells*, 87:117–131, 2005.

[10] K. Fan, M. Liu, T. Peng, L. Ma, and K. Dai. Effects of paste components on the properties of screen-printed porous TiO_2 film for dye-sensitized solar cells. *Renewable Energy*, 35(2):555–561, 2010.

[11] A. Goetzberger, C. Hebling, and H.-W. Schock. Photovoltaic materials, history, status and outlook. *Materials Science and Engineering: R: Reports*, 40(1):1–46, 2003.

[12] M. Grätzel. Dye-sensitized solar cells. *Journal of Photochemistry and Photobiology C: Photochemistry Reviews*, 4(2):145–153, 2003.

[13] M. A. Green. Third generation photovoltaics: Ultra-high conversion efficiency at low cost. *Prog. Photovolt: Res. Appl.*, 9(2):123–135, 2001.

[14] M. A. Green. Third generation photovoltaics: solar cells for 2020 and beyond. *Physica E: Low-dimensional Systems and Nanostructures*, 14(12):65–70, 2002.

[15] B. A. Gregg. *Semiconductor Photochemistry and Photophysics*, chapter The essential interface: studies in dye-sensitized solar cells, pages 51–88. Marcel Dekker, 2003.

[16] A. Hagfeldt and M. Grätzel. Light-induced redox reactions in nanocrystalline systems. *Chemical Reviews*, 95:1:49–68.

[17] A. Hauch and A. Georg. Diffusion in the electrolyte and charge-transfer reaction at the platinum electrode in dye-sensitized solar cells. *Electrochimica Acta*, 46(22):3457–3466, 2001.

[18] X. Huang, P. Shen, B. Zhao, X. Feng, S. Jiang, H. Chen, H. Li, and S. Tan. Stainless steel mesh-based flexible quasi-solid dye-sensitized solar cells. *Solar Energy Materials and Solar Cells*, 94(6):1005–1010, 2010.

[19] R. Huber, J.-E. Moser, M. Grätzel, and J. Wachtveitl. Real-time observation of photoinduced adiabatic electron transfer in strongly coupled dye/semiconductor colloidal systems with a 6 fs time constant. *The Journal of Physical Chemistry B*, 106(25):6494–6499, 2002.

[20] R. Huffaker. Protecting water resources in biofuels production. *Water Policy*, 12(1):129–134, 2010.

[21] M. Ikegami, J. Suzuki, K. Teshima, M. Kawaraya, and T. Miyasaka. Improvement in durability of flexible plastic dye-sensitized solar cell modules. *Solar Energy Materials and Solar Cells*, 93:836–839, 2009.

[22] S. Ito, P. Chen, P. Comte, M. K. Nazeeruddin, P. Liska, P. Péchy, and M. Grätzel. Fabrication of screen-printing pastes from TiO_2 powders for dye-sensitised solar cells. *Progress in Photovoltaics: Research and Applications*, 15(7):603–612, 2007.

[23] S. Ito, T. Kitamura, Y. Wada, and S. Yanagida. Facile fabrication of mesoporous TiO_2 electrodes for dye solar cells: chemical modification and repetitive coating. *Solar Energy Materials and Solar Cells*, 76(1):3–13, 2003.

[24] S. Ito, M. K. Nazeeruddin, P. Liska, P. Comte, R. Charvet, P. Péchy, M. Jirousek, A. Kay, S. M. Zakeeruddin, and M. Grätzel. Photovoltaic characterization of dye-sensitized solar cells: effect of device masking on conversion efficiency. *Progress in Photovoltaics: Research and Applications*, 14(7):589–601, 2006.

[25] S. Ito, K. Takahashi, S. ich Yusa, T. Imamura, and K. Tanimoto. Effects of homogenization scheme of TiO_2 screen-printing paste for dye-sensitized solar cells. *International Journal of Photoenergy*, 2012:7, 2012.

[26] J. Jiang, G. Oberdörster, and P. Biswas. Characterization of size, surface charge, and agglomeration state of nanoparticle dispersions for toxicological studies. *Journal of Nanoparticle Research*, 11:77–89, 2009.

[27] X. Jiangeng. Perspectives on organic photovoltaics. *Polymer Reviews*, 50(4):411–419, 2010.

[28] A. Kay and M. Grätzel. Low cost photovoltaic modules based on dye sensitized nanocrystalline titanium dioxide and carbon powder. *Solar Energy Materials and Solar Cells*, 44(1):99–117, 1996.

[29] T. Kitamura, K. Okada, H. Matsui, and N. Tanabe. Durability of dye-sensitized solar cells and modules. *Journal of Solar Energy Engineering*, 132(2):5, 2010.

[30] H. Li, Z. Xie, Y. Zhang, and J. Wang. The effects of ethyl cellulose on PV performance of DSSC made of nanostructured ZnO pastes. *Thin Solid Films*, 518(24, Supplement):e68 – e71, 2010.

[31] M. Liberatore, F. Decker, L. Burtone, V. Zardetto, T. Brown, A. Reale, and A. Di Carlo. Using EIS for diagnosis of dye-sensitized solar cells performance. *Journal of Applied Electrochemistry*, 39:2291–2295, 2009.

[32] W. R. McNamara, R. C. Snoeberger III, G. Li, C. Richter, L. J. Allen, R. L. Milot, C. A. Schmuttenmaer, R. H. Crabtree, G. W. Brudvig, and V. S. Batista. Hydroxamate anchors for water-stable attachment to TiO_2 nanoparticles. *Energy Environ. Sci.*, 2(11):1173–1175, 2009.

[33] Z. Ning, Y. Fu, and H. Tian. Improvement of dye-sensitized solar cells: what we know and what we need to know. *Energy Environ. Sci.*, 3(9):1170–1181, 2010.

[34] B. O'Regan and M. Grätzel. A low-cost, high-efficiency solar cell based on dye-sensitized colloidal TiO_2 films. *Nature*, 353(6346):737–740, 1991.

[35] J. H. Park and N. R. Aluru. Temperature-dependent wettability on a titanium dioxide surface. *Molecular Simulation*, 35(1/2):31–37, 2009.

[36] S.-s. Park, E. Seon-mi, S. Dong Ho, and S. Yong-gun. Preparation of highly ordered TiO_2 nanotubes on Ti-foil for dye-sensitized solar cells. *Research on Chemical Intermediates*, 36(1):77–82, 2010.

[37] D. Riemer. The theoretical fundamentals of the screen printing process. *Microelectronics International Microelectronics International*, 6(1):8–17, 1989.

[38] J. D. Roy-Mayhew, D. J. Bozym, C. Punckt, and I. A. Aksay. Functionalized graphene as a catalytic counter electrode in dye-sensitized solar cells. *ACS Nano*, 4(10):6203–6211, 2010.

[39] C. S. Rustomji, C. J. Frandsen, S. Jin, and M. J. Tauber. Dye-sensitized solar cell constructed with titanium mesh and 3-D array of TiO_2 nanotubes. *The Journal of Physical Chemistry B*, 114(45):14537–14543, 2010.

[40] H. J. Snaith. How should you measure your excitonic solar cells? *Energy Environ. Sci.*, 2012.

[41] R. A. Spurr and H. Myers. Quantitative analysis of anatase-rutile mixtures with an X-ray diffractometer. *Anal. Chem.*, 29(5):760–762, May 1957.

[42] G. R. Timilsina, S. Mevel, and A. Shrestha. Oil price, biofuels and food supply. *Energy Policy*, 39(12):8098–8105, 2011.

[43] J.-C. Tinguely, R. Solarska, A. Braun, and T. Graule. Low-temperature roll-to-roll coating procedure of dye-sensitized solar cell photoelectrodes on flexible polymer-based substrates. *Semiconductor Science and Technology*, 26(4):1–6, 2011.

[44] UNEP. 21 issues for the 21st century: Result of the UNEP foresight process on emerging environmental issues. Technical report, United Nations Environment Programme (UNEP), 2012.

[45] J. Wang, N. R. Sottos, and R. L. Weaver. Tensile and mixed-mode strength of a thin film-substrate interface under laser induced pulse loading. *Journal of the Mechanics and Physics of Solids*, 52(5):999–1022, 2004.

[46] Q. Wang, J.-E. Moser, and M. Grätzel. Electrochemical impedance spectroscopic analysis of dye-sensitized solar cells. *The Journal of Physical Chemistry B*, 109(31):14945–14953, 2005.

[47] X. Wu, G. Q. M. Lu, and L. Wang. Shell-in-shell TiO_2 hollow spheres synthesized by one-pot hydrothermal method for dye-sensitized solar cell application. *Energy Environ. Sci.*, 4(9):3565–3572, 2011.

[48] D. Xie, S. Feng, Y. Lin, G. Dong, X. Xiao, X. Li, and X. Zhou. Preparation of porous nanocrystalline TiO_2 electrode by screen-printing technique. *Chinese Science Bulletin*, 52:2481–2485, 2007.

[49] S. Xu, C.-h. Zhou, Y. Yang, H. Hu, B. Sebo, B.-l. Chen, Q.-d. Tai, and X. Zhao. Effects of ethanol on optimizing porous films of dye-sensitized solar cells. *Energy & Fuels*, 25(3):1168–1172, 2011.

[50] Y. Yamamoto, M. Kawaraya, H. Segawa, S. Uchida, J. Kano, F. Saito, K. Tsujimoto, T. Saito, and S. Ito. 10% efficiency dye-sensitized solar cells using P25 TiO_2 nanocrystalline electrode prepared by a bead-milling method. *Chem. Lett. Chemistry Letters*, 40(11):1220–1222, 2011.

[51] A. Yella, H.-W. Lee, H. N. Tsao, C. Yi, A. K. Chandiran, M. Nazeeruddin, E. W.-G. Diau, C.-Y. Yeh, S. M. Zakeeruddin, and M. Grätzel. Porphyrin-sensitized solar cells with cobalt (II/III)-based redox electrolyte exceed 12 percent efficiency. *Science*, 334(6056):629–634, 2011.

[52] A. Yonezu, H. Cho, T. Ogawa, and M. Takemeto. Advanced indentation technique for strength evaluation of hard thin films. *Science and Technology of Advanced Materials*, 7(1):97–103, 2006.

[53] Q. Zhang. Personal communication, 2012.

[54] Y. Zhao, X. Li, Q. Li, and C. Deng. Enhancement of the photoelectric performance of dye-sensitized solar cells by sol-gel modified TiO_2 films. *Journal of Materials Science and Technology*, 27(8):764 – 768, 2011.

[55] D. Zhou, S. W. Bennett, and A. A. Keller. Increased mobility of metal oxide nanoparticles due to photo and thermal induced disagglomeration. *PLoS ONE*, 7(5):8, 2012.